Small-scale Helmholtz resonators with grazing turbulent boundary layer flow

Dacome, G.; Siebols, R.; Baars, W. J.

DOI
10.1080/14685248.2024.2412586

Publication date
2024

Document Version
Final published version

Published in
Journal of Turbulence

Journal of Turbulence

ISSN: (Print) (Online) Journal homepage: www.tandfonline.com/journals/tjot20

Small-scale Helmholtz resonators with grazing turbulent boundary layer flow

G. Dacome, R. Siebols & W.J. Baars

To cite this article: G. Dacome, R. Siebols & W.J. Baars (11 Oct 2024): Small-scale Helmholtz resonators with grazing turbulent boundary layer flow, Journal of Turbulence, DOI: 10.1080/14685248.2024.2412586

To link to this article: https://doi.org/10.1080/14685248.2024.2412586

Published online: 11 Oct 2024.

JOURNAL OF TURBULENCE
https://doi.org/10.1080/14685248.2024.2412586

Taylor & Francis
Taylor & Francis Group

Small-scale Helmholtz resonators with grazing turbulent boundary layer flow

G. Dacome, R. Siebols and W.J. Baars

Department of Flow Physics & Technology, Faculty of Aerospace Engineering, Delft University of Technology, Delft, The Netherlands

ABSTRACT

Helmholtz resonators flush-mounted in a wall beneath turbulent boundary layer flow are studied by focusing on their flow-induced excitation and effect on the grazing turbulent flow. A particular focus lies on single resonators tuned to the most intense spatio-temporal fluctuations in the near-wall vertical velocity and wall-pressure, residing at a spatial scale of $\lambda_x^+ \approx 250$ (or temporal scale of $T^+ \approx 25$). Resonators are examined in a boundary layer flow at $Re_\tau \approx 2280$. Two neck-orifice diameters of $d^+ \approx 68$ and 102 are considered, and for each value of d^+ three different resonance frequencies are studied (corresponding to a period of $T^+ \approx 25$, as well as one lower, and one higher, period). The response of the TBL flow is analysed by employing velocity data from hot-wire anemometry and particle image velocimetry measurements. Passive resonance only affects streamwise velocity fluctuations in the region $y^+ \lesssim 25$, while vertical velocity fluctuations due to resonance reach up to $y^+ \approx 100$. A narrow-band increase in streamwise turbulence kinetic energy at the resonance scale co-exists with a more than 20% attenuation of lower-frequency energy. Current findings on single resonator cases will aid in the development of passive surfaces with distributed resonators for boundary-layer flow control.

ARTICLE HISTORY
Received 14 April 2024
Accepted 25 September 2024

KEYWORDS
Wall-bounded turbulence; Helmholtz resonator; acoustic resonance; flow manipulation

1. Introduction

Within turbulent boundary layer (TBL) flow, turbulence kinetic energy (TKE) production and transport mechanisms have been linked to mean surface quantities such as the wall-shear stress (and heat transfer rate in aerothermal flows). For flow control of surface quantities, *passive* methods are preferred based on practicality. Given that there is a growing body of knowledge suggesting that surface-embedded Helmholtz resonators (HRs) can substantially alter the kinetic energy of grazing wall-bounded turbulence, our current work investigates the interaction of a small-scale resonators and the grazing flow. Through our study, we reveal the response of a single resonator – tuned to the intense spatio-temporal fluctuations in the near-wall vertical velocity and wall-pressure – and examine the changes in local wall-impedance and the grazing velocity fluctuations. Results on this are valuable in the context of small-scale resonators being considered as meta-unit in future developments of passive surfaces for boundary-layer flow control.

Throughout this manuscript, coordinates x, y and z are employed to denote the streamwise, wall-normal and spanwise directions of the flow, respectively. Corresponding quantities u, v, w and p represent the Reynolds-decomposed fluctuations of velocity and pressure. The friction Reynolds number $Re_\tau \equiv \overline{U}_\tau \delta/\nu$ is the ratio of the inertial length scale (the boundary layer thickness, δ) to the viscous length scale, $l^* = \nu/\overline{U}_\tau$, where ν is the kinematic viscosity and $\overline{U}_\tau = \sqrt{\tau_w/\rho}$ is the friction velocity (here τ_w is the wall-shear stress (WSS) and ρ is the fluid density). When a length is scaled with the viscous length l^*, when time is scaled with $\nu/\overline{U}_\tau^2$, and when a velocity is normalised with $\overline{U}_\tau$, the quantity is presented with a superscript '+'.

1.1. Influencing the near-wall cycle of turbulent boundary layer flow

For fully developed wall-bounded turbulence, a self-sustaining cycle of turbulence very near the wall has a well-imprinted signature in the energy spectra of velocity fluctuations [1–4]. In a premultiplied energy spectrogram of u, denoted as $k_x\phi_{uu}(\lambda_x, y)$, the well-known inner-spectral peak appears at $(\lambda_x^+, y^+) \approx (10^3, 15)$

CONTACT W.J. Baars w.j.baars@tudelft.nl

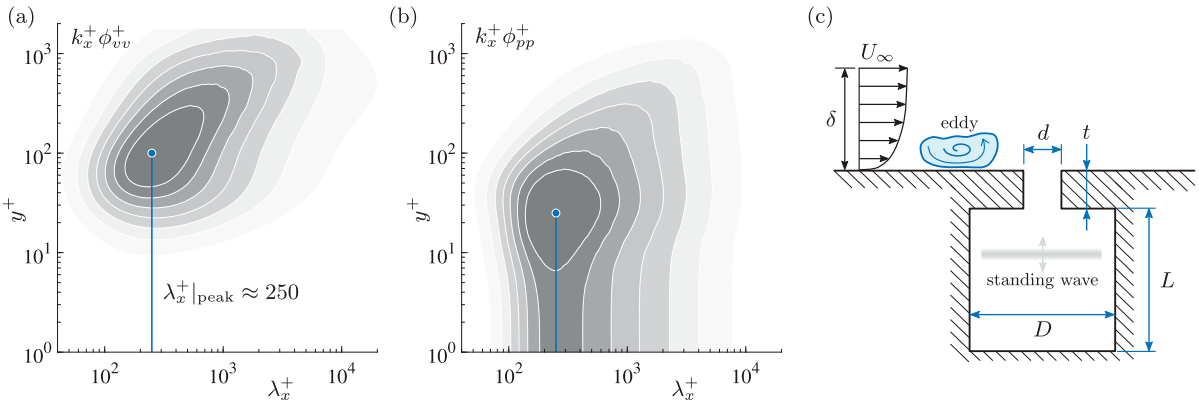

Figure 1. Spectrograms of (a) the *v* fluctuations, and (b) the *p* fluctuations, as a function of the streamwise wavelength λ_x and wall-normal distance *y*. These data are taken from a DNS of turbulent channel flow at $Re_\tau \approx 2000$ [6]. Grey-filled iso-contours correspond to levels of (**a**) $k_x^+\phi_{vv}^+ = [0.05 : 0.05 : 0.35]$, and (**b**) $k_x^+\phi_{pp}^+ = [0.40 : 0.40 : 2.80]$. (c) Schematic illustration of a cylindrical HR beneath a grazing TBL flow.

and is Reynolds number invariant [5]. For the wall-normal velocity fluctuations, the peak energy in $k_x\phi_{vv}$ resides at a higher position and at smaller wavelengths, as seen from the peak at $(\lambda_x^+, y^+) \approx (250, 100)$ in Figure 1(a). This spectrogram is inferred from Direct Numerical Simulation (DNS) data of turbulent channel flow [6] and corresponds to $Re_\tau \approx 2000$ (close to the Reynolds number of our current work). When considering the pressure fluctuations *p*, the primary hump of energy in $k_x\phi_{pp}$ resides at $(\lambda_x^+, y^+) \approx (250, 25)$ [7]. Clearly, $k_x\phi_{pp}$ remains constant for $y^+ \lesssim 5$ and approaches the wall-pressure spectrum. Furthermore, it has been shown that the inner-spectral peaks of the fluctuations in pressure and vertical velocity are Reynolds-number invariant and remain fixed at $\lambda_x^+ \approx 250$ [6,8,9]. This property is relevant in the context of our study, since near-wall pressure and vertical velocity fluctuations couple to the dynamics of the HRs to-be-studied.

In the near-wall region, energy in the spectrogram is tied to a re-occurring bursting process [10,11] including ejection (Q2) and sweep (Q4) events; the latter are responsible for the largest contribution to the turbulence skin friction [12–14]. With increasing Re_τ, hairpin eddies become more pronounced, forming vortex packets [15] and co-existing large-scale motions [16], all of which are interlinked [17]. In the current work, we confine ourselves to the near-wall turbulence. The wall-bounded turbulence community has a relatively firm understanding of how to control near-wall flow mechanisms responsible for generating skin-friction drag. For instance, much research has gone into the development of passive techniques, such as micro-textured riblet-surfaces [18–20, amongst others]. Riblets with a size of $\mathcal{O}(10l^*)$ reduce drag [21–23], whereas larger riblets lead to an increase in drag due to roughness effects. Benefits similar to those provided by properly sized riblets can potentially be achieved with porous substrates comprising a large anisotropy [24–26]; these offer promising research pathways for advancing passive flow-control surfaces.

Our study revolves around a sub-surface unit-texture as a building block for another type of near-wall flow control surface. The unit considered is a small-scale resonator. In this regard, Choi and Fujisawa [27] showed that a single rectangular cavity of size $180 < d^+ < 240$ (where $d^+ = d/l^*$ is the dimension of the cavity cut-out) can yield a small net drag reduction. Silvestri et al. [28] hypothesised based on work of micro-perforated panel absorbers [29] that wall-embedded micro-cavities (circular blind holes) could '*dampen the coherent structures and disrupt the bursting cycle, which is responsible for the shear stress and viscous drag [...]*'. After a parametric sweep of cavity diameters, $(20 < d^+ < 150)$, a case with $d^+ \approx 60$ resulted in an optimum of streamwise TKE-attenuation (roughly 13%). In follow-up research to the micro-cavities with blind holes, Silvestri et al. [30,31] found that increasing the volume of a single backing cavity – to which all holes were connected – could further reduce the streamwise TKE. WSS modifications were primarily analysed by way of indirect methods, e.g. through a Clauser chart technique applied to the mean velocity profile or through an assessment of surrogate metrics from variable interval time-averaging (VITA) analysis of *u* time series [28,30–33]. Indirect methods can be inaccurate due to the lag in adjustment of the logarithmic velocity profile to a new wall-boundary condition [34]. However, conclusions stating that micro-cavities have the ability to reduce the WSS are consistent with the conclusive DNS study of Bhat et al. [35], who replicated the flow over a micro-cavity array with a single backing cavity [30]. Though, in all of the aforementioned studies, the

aspect of resonance was not considered. Hence, this study focuses on the interplay between a single small-scale resonator and the grazing turbulent velocity fluctuations.

1.2. Fundamentals of Helmholtz resonators

A brief review of the resonators is provided to allow for interpretation of the results in §§ 4–5. A cylindrical HR is shown in Figure 1(c) and its geometry is characterised by four parameters: the orifice diameter d and thickness t of the neck, and the diameter D and depth L of the cavity. Helmholtz formulated an expression for the resonance frequency when subject to acoustic pressure waves in the absence of grazing flow [36]:

$$f_r = \frac{a_0}{2\pi}\sqrt{\frac{S}{V_c\,(t+t^*)+P}}. \tag{1}$$

Here, $S = \pi d^2/4$ is the area of the orifice and $V_c = \pi D^2 L/4$ is the volume of the cavity. Parameter a_0 signifies the sound speed. Terms P and t^* are 'end-corrections' and account for the fact that not only the fluid medium within the neck oscillates vertically, but also a small portion of fluid inside the cavity and outside of the orifice. Different end-corrections can be found in the literature on acoustic resonators (e.g. [37,38]). Based on a wave-tube analysis, Panton and Miller [39] showed that Equation (1) with $P = 0$ is only valid when L is smaller than 1/16th of the acoustic wavelength. To account for longer cavities, they proposed the correction term $P = L^2 S/3$, which is adopted in our current work. The lumped end-correction of Ingard [38], $t^* = t^*_{\text{in}} + t^*_{\text{out}} = 0.48\sqrt{S}(1 - 1.25d/D) + 0.48\sqrt{S}$ (valid for $d/D < 0.4$), was shown to work well for design and is also adopted here (note that t^*_{in} and t^*_{out} refer to the portions of fluid inside the cavity and outside of the orifice, respectively). All in all, the true end-correction may vary based on the orifice geometry, cavity geometry and properties of the grazing flow.

A relation between the pressure at the neck-inlet (p_i, see the inset of Figure 2(a)) and in the cavity (p_c) is modelled through an input-output transfer kernel, H_r, by considering a mass-spring-damper system analogy. Its gain and phase are given by,

$$|H_r\,(f)\,| = \left[\left(1 - \left(\frac{f}{f_r}\right)^2\right)^2 + \left(\frac{2\xi f}{f_r}\right)^2\right]^{-\frac{1}{2}}, \quad \text{and} \tag{2a}$$

$$\varphi\left[H_r\,(f)\right] = -\tan^{-1}\left[\frac{2\xi\,(f/f_r)}{1-(f/f_r)^2}\right]. \tag{2b}$$

with ξ being the damping constant and f_r being the resonance frequency. While ξ must be determined empirically, f_r can be estimated using Equation (1). Though, after conducting a calibration experiment with an acoustic pressure-excitation (e.g. a broadband noise field) and simultaneous sampling of the inlet pressure p_i (input) and cavity pressure p_c (output), both ξ and f_r can be inferred from fitting Equations (2a) and (2b) to the measured gain and phase of the complex-valued kernel,

$$H_r^{\text{aco}}\,(f) = \frac{\langle P_c\,(f)\,P_i^*\,(f)\rangle}{\langle P_i\,(f)\,P_i^*\,(f)\rangle}. \tag{3}$$

Here the numerator is the input-output cross-spectrum and the denominator is the input spectrum. A capital symbol indicates the Fourier transform, e.g. $P_c(f) = \mathcal{F}[p_c(t)]$. A sample bode plot of Equation (3) is drawn in Figure 2(a). When a HR is subject to a harmonic wave of frequency $f \ll f_r$, the cavity pressure responds in-phase and the gain tends towards unity for low frequencies. For $f \gg f_r$, an out-of-phase behaviour is present and the fluid medium is subject to more friction, causing a rapid gain-decrease.

Finally, an acoustic impedance at the neck-inlet relates the inlet pressure of an acoustic resonator to the co-located velocity disturbance. Impedance is expressed as $Z_i \equiv P_i(f)/V_i(f)$, where $V_i(f) = \mathcal{F}[v_i(t)]$ is the temporal Fourier transform of the vertical velocity signal, and $v_i > 0$ corresponds to an upward neck-inlet velocity (a motion of the air mass in the resonator's neck in the positive y direction). A typical bode plot with the gain and phase of Z_i is drawn in Figure 2(b). Its general characteristics are based on theory of which all

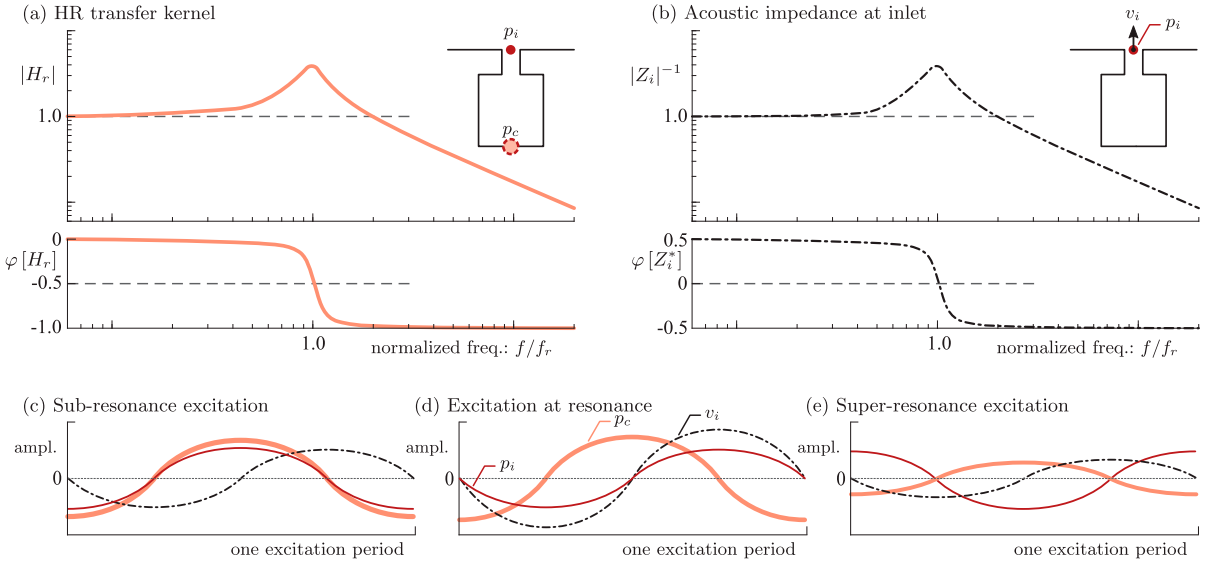

Figure 2. Bode plot with gain and phase of (a) the HR transfer kernel between the inlet and cavity pressures, and (b) the acoustic impedance at the neck-inlet between the co-existing pressure and vertical velocity. (c,d,e) Illustrations over one excitation period, of the temporal fluctuations of p_i, p_c and v_i for a pure acoustic resonator with sub-resonance excitation, excitation at resonance, and super-resonance excitation, respectively.

details can be found in literature [40]. At sub-resonance excitation ($f \ll f_r$), the inlet pressure is compliant with the inlet velocity: when the mass of air moves inside ($v < 0$) the air is compressed and the applied inlet pressure is a quarter-period ahead of the vertical velocity. Conversely, at super-resonance excitation ($f \gg f_r$), acoustic inertance manifests itself and the applied inlet pressure signal lags a quarter-period behind the vertical velocity. At resonance, $|Z_i|$ is low and maximum flow into and out of the resonator occurs with zero-phase delay between p_i and v_i. Temporal fluctuations of p_i, p_c and v_i are summarised in Figure 2(c–e) for a pure acoustic resonator with sub-resonance excitation, excitation at resonance, and super-resonance excitation, respectively.

1.3. Helmholtz resonators and grazing flow

Only very few studies consider a HR for control of grazing flow. Laminar flow control studies [41,42] were aimed at attenuating convective Tollmien-Schlichting (TS) waves that are nearly harmonic. Michelis et al. [41] concluded that pressure perturbations in the HR behave acoustically and that f_r is unaltered when excited by TS waves rather than acoustic waves. Furthermore, only an *amplification* of the TS waves was achieved with a single degree-of-freedom HR. This is because the wall-normal velocity perturbation of the resonator is, on average, amplifying wall-normal velocity fluctuations of the convective TS wave (the phase relation established by the passive resonator does not yield an opposing perturbation). Phononic crystals offer a more promising route in this regard, since a wider design space allows for tuning the phase between free-face surface displacements and the wall-pressure [43].

For TBL flow, studies cover a wide variety of HR sizes. Wall-bounded flows are often studied over (resonating) cavities that span multiple δ [44–49]. Response of the boundary layer flow downstream is not the focus of such studies, but rather properties of the Kelvin–Helmholtz (KH) and/or Rossiter modes of the shear layer. Some studies do consider arrays of HRs for separation control [50,51]. Again, many of these consider large-scale resonators of size $\mathcal{O}(\delta)$ [52–55], and are aimed at (global) flow separation control. Moreover, none of the aforementioned studies consider tuning the HR to characteristics of the incoming flow. Panton and Miller [56] were the first to do so by tuning relatively small HRs to different portions of the wall-pressure spectrum, while exclusively focusing on their acoustic response. How the HR affected the TBL flow was addressed in follow-up work [57–59], where they observed increased $\overline{u^2}^+$ and $\overline{v^2}^+$ stresses, with smaller changes in the Reynolds shear stress ($-\overline{uv}^+$). No further data analysis was presented on the attenuation/amplification of specific ranges of scales in the grazing flow.

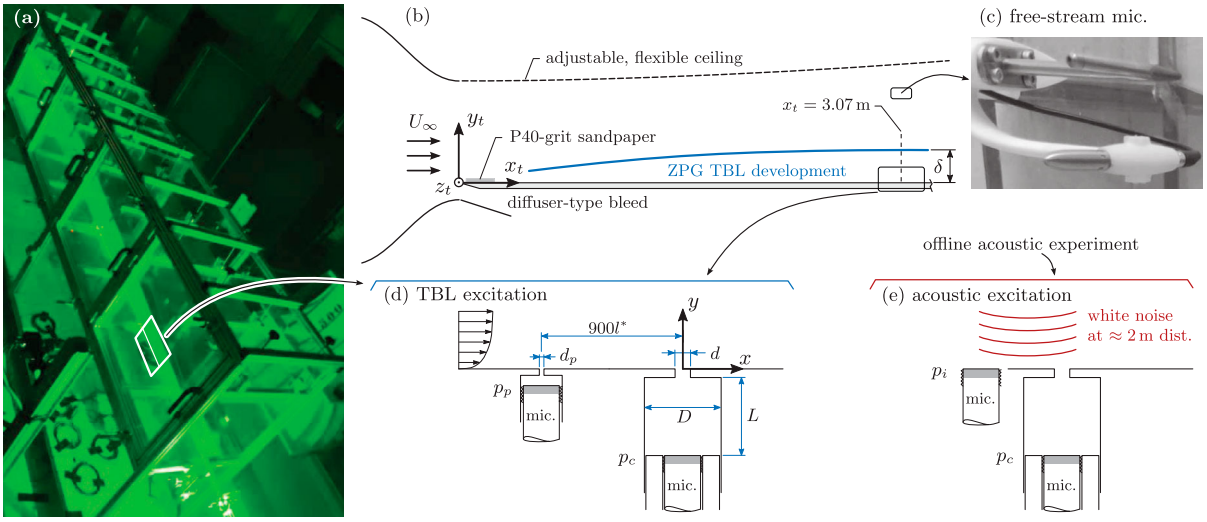

Figure 3. (a,b) Setup for the TBL studies in the W-tunnel. (c) Photograph of the Pitot-static tube and microphone situated in the potential flow region. (d) Detail of a wall-embedded HR at $x = 0$, and a pinhole-mounted microphone located upstream for wall-pressure measurements. (e) Arrangement for acoustic characterisation of a HR.

Our current work is exclusively focused on grazing TBL flow over a small-scale, single degree-of-freedom HR. The concept of 'small-scale' refers to a miniature resonator of which the neck orifice diameter is $\mathcal{O}(10l^*)$, and the resonance frequency coincides closely with the inner spectral-peak. Contrary to what occurs in laminar flows with TS waves [41], incoming pressure and velocity fluctuations are broadband and possess a non-deterministic phase. From a resolvent-modelling perspective, frequency-tuned surfaces have shown promise for passive flow control of the non-deterministic wall-bounded turbulence [60]. That is, both the near-wall cycle and larger-scale motions could be suppressed, however, (meta)surfaces would have to be developed to obtain the desired wall-impedance. Our work is aimed at contributing towards inferring how a resonator changes the wall-impedance and grazing flow dynamics.

This work is structured as follows. First a brief overview of the experimental methodology is provided in § 2, as well as the characteristics of our baseline TBL flow. Then, in § 3, we cover the design philosophy of the small-scale resonators, followed by an overview of their response to TBL flow- and acoustic-excitation scenarios in § 4. Details on the response of the TBL flow are presented in § 5.

2. Turbulent boundary layer flow and experimental methodology

2.1. Facility and instrumentation

Experiments were conducted in an open-return wind tunnel facility at the Delft University of Technology. A brief overview of the facility and instrumentation is here provided, while further details are found in Baars et al. [61].

For generating the TBL flow, a setup with a relatively long streamwise development length was employed (Figure 3(a,b)): the bottom wall, over which the boundary layer developed under zero-pressure gradient (ZPG) conditions, has a length of 3.75 m and spans 0.60 m in width. The TBL was initiated just downstream of the leading edge at $x_t = 0$, with a P40-grit sandpaper-trip applied on all four surfaces of the test section. Measurements are performed near the downstream end of the setup, around $x_t = 3.07$ m. A coordinate system (x, y, z) is used for the presentation of results in later sections, and has its origin at the midpoint of the HR orifice (see Figure 3(d)).

Single HRs were flush-mounted at the spanwise centre of the test section. Fluctuating pressure measurements were conducted with three sensors: with a pressure-microphone at the bottom of the HR cavity (p_c) to measure cavity-pressure, with a microphone mounted behind a pinhole upstream (p_p) to infer wall-pressure, and with a microphone in the potential flow region (p_f), near the Pitot-static tube (see photo in Figure 3(c)), to record facility acoustic noise. All three microphones were GRAS 46BE $\frac{1}{4}$ in. CCP free-field

ones, with the grid caps removed. Only for the microphone measuring p_f, a GRAS RA002 nosecone was added to remove pressure fluctuations from free-stream turbulence. The microphone sets have a frequency response range with an accuracy of ± 1 dB for 10 Hz to 40 kHz, with a nominal sensitivity of 3.6 mV/Pa (*in-situ* sensitivities were inferred with the aid of a GRAS 42AG calibrator). The dynamic range is 35 dB to 160 dB (with a reference pressure of $p_{\text{ref}} = 20\,\mu\text{Pa}$). Regarding the measurement of wall-pressure, a pinhole-configuration was employed to enhance the spatial resolution of the measurement. That is, the microphone diaphragm is relatively large (~ 6 mm in diameter) and the conventional method to enhance spatial resolution is to embed the sensor at the bottom of a micro-cavity behind a pinhole [62]. The pinhole diameter of $d_p = 0.5$ mm ($d_p^+ \approx 16$) is of an acceptable value for a fully-resolved wall-pressure measurement [63]. Since the combination of a pinhole and sub-surface cavity of the pinhole-mounted microphone behaves like a HR itself, the measured pressure p_p can be corrected so that it reflect the true wall-pressure, p_w, at the pinhole-inlet. This correction requires removal of facility acoustic noise, using p_f, and a transfer kernel of the pinhole/cavity geometry determined from an acoustic excitation experiment. Resonance of the pinhole/cavity geometry was identified at roughly 4 kHz and this is beyond the energetic temporal scales of interest in the wall-pressure, thus yielding a minor correction, all details of which can be found in literature [61]. In the remainder of this work we proceed using the inferred wall-pressure, p_w, at the pinhole location ($x = -900l^*$).

Boundary layer turbulence was captured using hot-wire anemometry (HWA) and particle image velocimetry (PIV) measurements. For the former, a TSI IFA-300 bridge was used in CTA mode together with a Dantec 55P15 miniature-wire boundary layer probe. Its sensing length is $l = 1.25$ mm (equating to $l^+ \approx 42.4$ for the TBL flow tested) with a length-to-diameter ratio of $l/d_w = 250$. One wall-normal profile was acquired without HR installed, to infer baseline TBL characteristics. This profile was acquired with 40 points logarithmically spaced in the range $y^+ \in (10, 2800)$, at $x^+ \approx -1695$ (results shown in § 2.2). For the cases with HRs installed, profiles were acquired only at $x^+ \approx 186$, with 20 points logarithmically spaced in the range $y^+ \in (7, 100)$. All time series of HWA voltage and microphone signals were sampled at a rate of $\Delta T^+ \equiv \overline{U}_\tau^2/\nu/f_s = 0.36$ ($f_s = 51.2$ kHz is the sampling frequency) and for an uninterrupted duration of $T_a = 60$ seconds ($T_a\overline{U}_\infty/\delta \approx 13{,}200$). Finally, the hot-wire probe was calibrated *in-situ* using the reference velocity provided by the Pitot-static tube; corrections for hot-wire voltage drift were also implemented [64].

Planar two-dimensional two-component (2D2C) PIV measurements were conducted in the (x, y) plane. One LaVision Imager sCMOS camera was used with a 16-bit CCD sensor, with a size of 2560×2160 px^2 and 6.5 μm pixel size. A Nikon lens with a 60 mm focal length and an f# of 8 was employed. A 1 mm thick sheet was illuminated by a double cavity Quantel Evergreen EVG00200 Nd:YAG laser, with a maximum energy per pulse of 200 mJ. Flow tracers were generated with the aid of an atomised glycol-water mixture, yielding an average particle size of around 1 μm. Measurements captured a field-of-view (FOV) surrounding the HR orifice at $x = 0$, with a streamwise and wall-normal extent of roughly 1.45δ and 1.20δ, respectively (image resolution of 26 px/mm). Image pairs were acquired with a frame-delay of 35 μs, and for each dataset a total of two sets of 2000 statistically independent images were acquired at a rate of 15 Hz. For conditional averaging 4000 velocity fields to phases in the cavity pressure oscillations, the laser Q-switch of the first pulse was acquired synchronously with the microphone signals p_c, p_p and p_f. PIV processing was performed with LaVision DaVis 10.2. First, the average velocity field was computed from a coarse single-pass processing, with an interrogation window size 96×96 px^2. After pre-shifting images with the aid of this average shear-flow field, a multi-pass cross-correlation was performed with as a first pass a 24×24 px^2 window, and as a final pass a 12×12 px^2 window with 50% overlap. With a uniform seeding density of ~ 0.035 particles-per-pixel (ppp), this final window of 12×12 pixels^2 included ~ 5 particles on average. A final vector pitch of 0.23 mm ($7.8l^*$) was obtained, and this was deemed to be sufficient for capturing the inflow/outflow phenomena (approximately 9 vectors spanning the resonator's neck-diameter of $d = 68l^*$).

2.2. Turbulent boundary layer characteristics

A baseline mean velocity profile (MVP) and streamwise TKE profile are presented in Figure 4(a). Boundary layer parameters are listed in Table 1 and were obtained by fitting the MVP to a composite profile with log.-law constants of $\kappa = 0.384$ and $B = 4.17$ [65]. On the basis of these values the friction Reynolds number

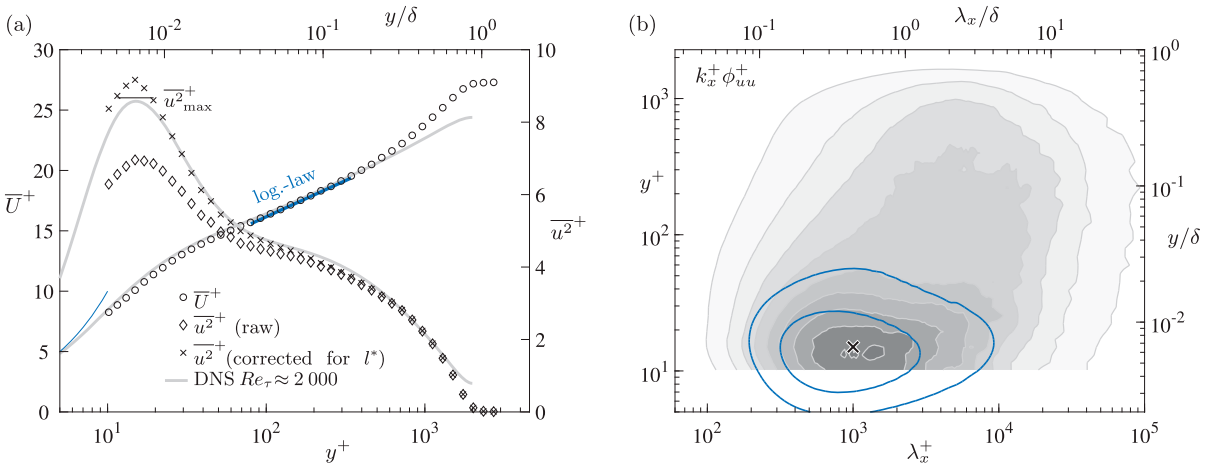

Figure 4. (a) Streamwise MVP and streamwise TKE profile of the baseline TBL flow. Both are compared to DNS data of turbulent channel flow at $Re_\tau \approx 2000$ [6]. The MVP is compared to the logarithmic law with constants $\kappa = 0.384$ and $B = 4.17$. The streamwise TKE profile is corrected for spatial resolution effects. (b) Premultiplied energy spectrogram $k_x^+\phi_{uu}^+$ (filled iso-contours 0.2:0.2:1.8); note that $\lambda_x = \overline{U}_c(y)/f$. Overlaid are two iso-contours inferred from the DNS data and correspond to levels of $k_x^+\phi_{uu}^+ = [1.0; 1.6]$.

Table 1. Experimental parameters of the baseline TBL flow in the W-tunnel, inferred from a mean velocity profile acquired with HWA at $x = -50$ mm (just upstream of where the HR is placed).

Re_τ	Re_θ	$\overline{U}_\infty$ (m/s)	δ (mm)	θ (mm)	$\overline{U}_\tau$ (m/s)	$l^* \equiv \nu/\overline{U}_\tau$ (μm)	$\nu/\overline{U}_\tau^2$ (μs)	Π	x^+ location
2280	6190	14.8	67.3	6.71	0.54	29.50	54.56	0.56	−1695

is $Re_\tau \approx 2280$. Our MVP agrees well with the DNS data of turbulent channel flow at $Re_\tau \approx 2000$ [6], up to the wake-region. An attenuation of the streamwise TKE is observed due to the hot-wire's spatial resolution limit [66]. After correcting for the missing energy with the method by Smits et al. [67] (applicable at the current value of Re_τ and for the canonical, ZPG boundary layer flow), the current streamwise TKE profile agrees well with the DNS profile in the buffer region and above. Note that in the remainder of this paper we consider uncorrected data, since the case with the HR is no longer producing a canonical, equilibrium TBL flow (rendering the method of Smits et al. [67] inapplicable). Even though more generalised correction methods exist (e.g. [68]), they rely on data from probes with different spatial resolutions. Moreover, we do not require a correction because the measurement resolution is still sufficient to resolve the near-wall cycle scales [66], and because our study concentrates on energy differences between – what has been confirmed to be – a proper baseline flow and the one grazing the resonator. And so, for each dataset of a HR case, an accompanied dataset of the baseline flow is available (acquired with the exact same instrumentation).

For evaluating the spectral content of the HWA data, one-sided spectra are taken as $\phi_{uu}(y;f) = 2\langle U(y;f)U^*(y;f)\rangle$, where $U(y;f) = \mathcal{F}[u(y,t)]$ is the temporal FFT. Here, the angular brackets $\langle\cdot\rangle$ denote ensemble averaging, and superscript $*$ signifies the complex conjugate. Ensemble averaging is performed using FFT partitions of $N = 2^{12}$ samples (subject to a Hanning window), resulting in a spectral resolution of $\mathrm{d}f = 12.5$ Hz with 1500 ensembles and 50% overlap. For interpretative purposes, frequency spectra are converted to wavenumber spectra using a convection velocity $\overline{U}_c(y)$, taken according to the local mean velocity except for $y^+ \lesssim 10$ where the convection velocity plateaus to a constant value of $\overline{U}_c^+ = 10$ according to Figure 3 of Liu and Gayme [69]. With streamwise wavenumber $k_x = 2\pi f/\overline{U}_c$ the premultiplied spectra, $k_x\phi_{uu}(k_x)$, are presented in terms of a wavelength on the scale axis, thus $\lambda_x = 2\pi/k_x = \overline{U}_c/f$. A streamwise energy spectrogram is shown in Figure 4(b) with the inner-spectral peak residing around $(\lambda_x^+, y^+) = (10^3, 15)$. Having established the presence of a baseline TBL flow with a representative mean velocity profile, and streamwise Reynolds stress characteristics, we proceed with the description of the HR design.

Table 2. Geometric parameters and resonance frequencies for each Helmholtz resonator (HR).

Resonator	d^+	d (mm)	t (mm)	D (mm)	L (mm)	Label	f_r (Hz)	f_r^+	$\lambda_{x,r}^+$	λ_a/L	f_r^{aco} (Hz)	ξ^{aco}	f_r^{tur} (Hz)	ξ^{tur}
$\mathcal{R}1$	68	2.0	4.0	11.0	48.0	$\mathcal{LF}$	581	0.032	315	12.4	576	0.125	631	0.192
					24.0	$\mathcal{NF}$	843	0.046	217	17.1	833	0.166	853	0.132
					8.0	$\mathcal{HF}$	1485	0.081	123	29.1	1446	0.193	1385	0.145
$\mathcal{R}2$	102	3.0	4.0	11.0	80.0	$\mathcal{LF}$	585	0.032	313	7.4	584	0.062	622	0.084
					48.0	$\mathcal{NF}$	794	0.043	231	9.1	794	0.080	833	0.081
					16.0	$\mathcal{HF}$	1454	0.079	126	14.9	1464	0.099	1413	0.084

Design frequencies f_r are converted to a streamwise wavelength using $\lambda_{x,r}^+ \equiv \overline{U}_c^+/f_r^+$ and a convection velocity of $\overline{U}_c^+ = 10$. Cavity depths L are compared to the acoustic wavelength $\lambda_a \equiv a_0/f_r$ in the column listing λ_a/L.

3. Resonator design and sizing

When sizing a HR both spatial and temporal scales need to be decided upon. We only consider a cylindrical HR (Figure 1(c)) and for its spatial scale the orifice diameter d is the leading parameter because it dictates the size of the interface between the grazing flow and the HR. A temporal scale is imposed by the resonance frequency, f_r. This work considers two HRs, for which d and f_r are chosen in such a way that the HR at resonance interacts with the most energetic near-wall content.

Regarding ***spatial tuning***, Panton and Miller [56] emphasised that a maximum intensity of self-resonance is achieved when the turbulence excitation (e.g. a characteristic eddy size of a normal velocity fluctuation or pressure-event) is twice the orifice diameter, d. It was conjectured that this creates a pronounced *inflow* and *outflow* phase when convecting past the orifice, assuming that a shear-layer instability over the orifice does not play a major role. We proceed with the same assumption, and we will in fact confirm whether HRs resonate according to acoustic theory. Both v and p events are most energetic at a characteristic scale of $\lambda_x^+ = 250$ (Figure 1(a,b)), and in a view of perfect periodicity this equates to event sizes of $\Delta x^+ = 125$. Two HRs with orifice diameters of $d^+ = 68$ ($d = 2$ mm) and $d^+ = 102$ ($d = 3$ mm) are investigated, of which all parameters are listed in Table 2; we refer to these with $\mathcal{R}1$ and $\mathcal{R}2$, respectively. For $\mathcal{R}1$, the near-wall scales are almost twice the size of the orifice diameter, following Panton and Miller [56]. The larger diameter orifice is still below the characteristic scale of an excitation event, and is of interest since a larger orifice diameter results in less viscous losses in the neck (for the same neck thickness, which was kept constant at $t = 4$ mm) and thus a stronger resonance. Preliminary studies also considered a smaller orifice of $d^+ = 36$ ($d = 1$ mm), but no effect on the TBL flow was observed, hence this case is omitted.

When considering ***temporal tuning***, the resonance frequency f_r is adjusted by varying the cavity depth, L. For all resonators the cavity diameter is held constant at $D = 11$ mm to accommodate the microphone for measuring the cavity pressure, p_c. Three different frequencies are considered. First, a nominal resonance frequency matches the dominant scale in v and p fluctuations ($\lambda_x^+ = 250$). With $\overline{U}_c^+ = 10$, the target frequency becomes $f^+ = \overline{U}_c^+/\lambda_x^+ = 0.04$. Note that this equates to the peak-frequency in wall-pressure spectra from temporal data [9] over a large range of Reynolds numbers. With d, t and D being fixed, L is designed according to Equation (1) with the correction terms t^* and P described in § 1.2. This case is referred to as the nominal frequency ($\mathcal{NF}$) case and Table 2 lists all relevant parameters. For ease of manufacturing L was rounded and results in slight changes in the design resonance frequency. For each resonator, two additional design frequencies are considered and these are referred to as low- and high-frequency cases ($\mathcal{LF}$ and $\mathcal{HF}$, respectively). For the former, L is adjusted such that the spatial wavelength induced is a factor 1.5 larger than the most energetic wavelength. This results in $f_r^+ \approx 0.03$. Likewise, for the $\mathcal{HF}$ case, L is adjusted so that smaller spatial wavelengths are targeted (higher frequencies, $f_r^+ \approx 0.08$). Our parameter sweep over frequency aims to test how the energetic near-wall cycle responds, on average, to an interaction with HRs that interact in-phase or out-of-phase with different portions of the wall-pressure spectrum.

4. Response of the Helmholtz resonators

Resonators are assessed in terms of their response to pure acoustic excitation, as well as to excitation with grazing TBL flow. The acoustic experiment was conducted in the A-tunnel facility of the Delft University of

Technology, which includes a test room that is anechoic at frequencies beyond 200 Hz [70]. White noise was produced with a Bose® speaker situated ≈ 2 m from the HR, and was configured so that the acoustic wave-fronts were co-planar with the orifice plane (Figure 3(e)). Noise recordings were made using two microphones similar to the ones described in § 1.2: one captured the cavity pressure, p_c, and one was flush-mounted next to the HR orifice to directly capture the neck-inlet pressure, p_i. With recordings of $T_a \approx 120$ seconds and ensemble-averaging using FFT partitions of $N = 2^{13}$ samples (1500 ensembles with 50% overlap), a spectral resolution of $\mathrm{d}f = 6.25$ Hz was obtained for the HR transfer kernel H_r^{aco} given by Equation (3) (superscript 'aco' refers to the *acoustic* excitation).

Bode plots of H_r^{aco} for resonator $\mathcal{R}1$ are provided in Figure 5(a,b). The gain for all three resonance frequencies is presented with the three red curves at the bottom of Figure 5(a), while the corresponding phase curves are shown in Figure 5(b). Abscissae are normalised with the resonance frequency. Dark lines correspond to the measurements and are plotted for $f \gtrsim 100$ Hz only due to the non-anechoic nature of the facility at lower frequencies. The gain of Equation (2a) was fit to the measured gain by first identifying a peak frequency, f_p. Thereafter, a nonlinear least squares fit of the gain expression was performed in the range $f \in [f_p/1.75, 1.75f_p]$, using f_r and ξ as free parameters (the resulting gain and phase of the model kernel are plotted with the light-shaded lines). Bode plots for resonator $\mathcal{R}2$ are presented in an identical manner in Figure 5(c,d), and the inferred resonance frequencies and damping constants, f_r^{aco} and ξ^{aco}, respectively, are listed in Table 2.

Overall, the model transfer kernel represents the data fairly well up to two-to-three times the resonance frequency, after which overtones are occasionally present (particularly in the $\mathcal{LF}$ case of resonator $\mathcal{R}2$). Analytical solutions of such overtones can be found by solving the acoustic wave-tube equations [39]. It was confirmed that the predicted frequencies agree well to the overtones in the measurements [71]. Nevertheless, since overtones have a much weaker gain and occur at frequencies beyond the energetic scales of the turbulence, these tones are not further relevant.

Values of f_r^{aco} and ξ^{aco} are plotted in Figure 6(a,b) for both resonators with the red curves. The frequency ordinate is normalised with the design frequency in Figure 6(a). A shaded band around $f/f_r = 1$ indicates the expected variation in the resonance frequency due to temperature changes of ± 5 K (this changes the sound speed and hence the resonance frequency). Shaded bands around the data curves correspond to the 95% confidence interval of the nonlinear least squares to obtain f_r^{aco} and ξ^{aco}. Clearly, the HRs under acoustic excitation behave according to the acoustic design formulation, Equation (1). Resonance frequencies deviate less than 3%; such small discrepancies are ascribed to placement uncertainty of the cylindrical plug to adjust L. Damping constants follow the expected trends, in the sense that higher resonance frequencies and smaller neck diameter result in larger damping constants due to the acoustic particle velocities being subject to larger frictional losses.

Resonator excitation by the grazing TBL flow is considered next. The gain of the HR transfer kernel, H_r^{tur} (superscript 'tur' refers to the *turbulence* excitation), is determined from the HR cavity-pressure spectrum and the upstream wall-pressure spectrum, according to

$$|H_r^{\mathrm{tur}}(f)| = \left(\frac{\phi_{p_c p_c}(f)}{\phi_{p_w p_w}(f)} \right)^{\frac{1}{2}}. \tag{4}$$

Note that a phase of H_r^{tur} cannot be determined, since this requires the wall-pressure to be measured at $x = 0$, while the measurement sensor cannot be co-located with the HR orifice. Curves of the gain $|H_r^{\mathrm{tur}}|$ are plotted for both resonators in Figure 5(a,c) with the blue curves. After a fitting procedure identical to the one in the acoustic characterisation, the resonance frequency, f_r^{tur}, and damping constant, ξ^{tur}, are plotted in Figure 6(a,b) and listed in Table 2. It is apparent that the resonance frequency deviates more from the design frequency than in the case of acoustic excitation. For the $\mathcal{LF}$ case, the resonance frequency is higher than the design frequency and this switches to the resonance frequency being lower than the design frequency for the $\mathcal{HF}$ case (Figure 6(a)). This suggests that end-correction terms t^* and P are altered by the grazing flow. Nevertheless, the deviation is less than 10% for all cases, proving how Equation (1) is effectively valid not only for HR design in quiescent conditions, but also for one subject to TBL flow-excitation (within an uncertainty of $\sim 10\%$).

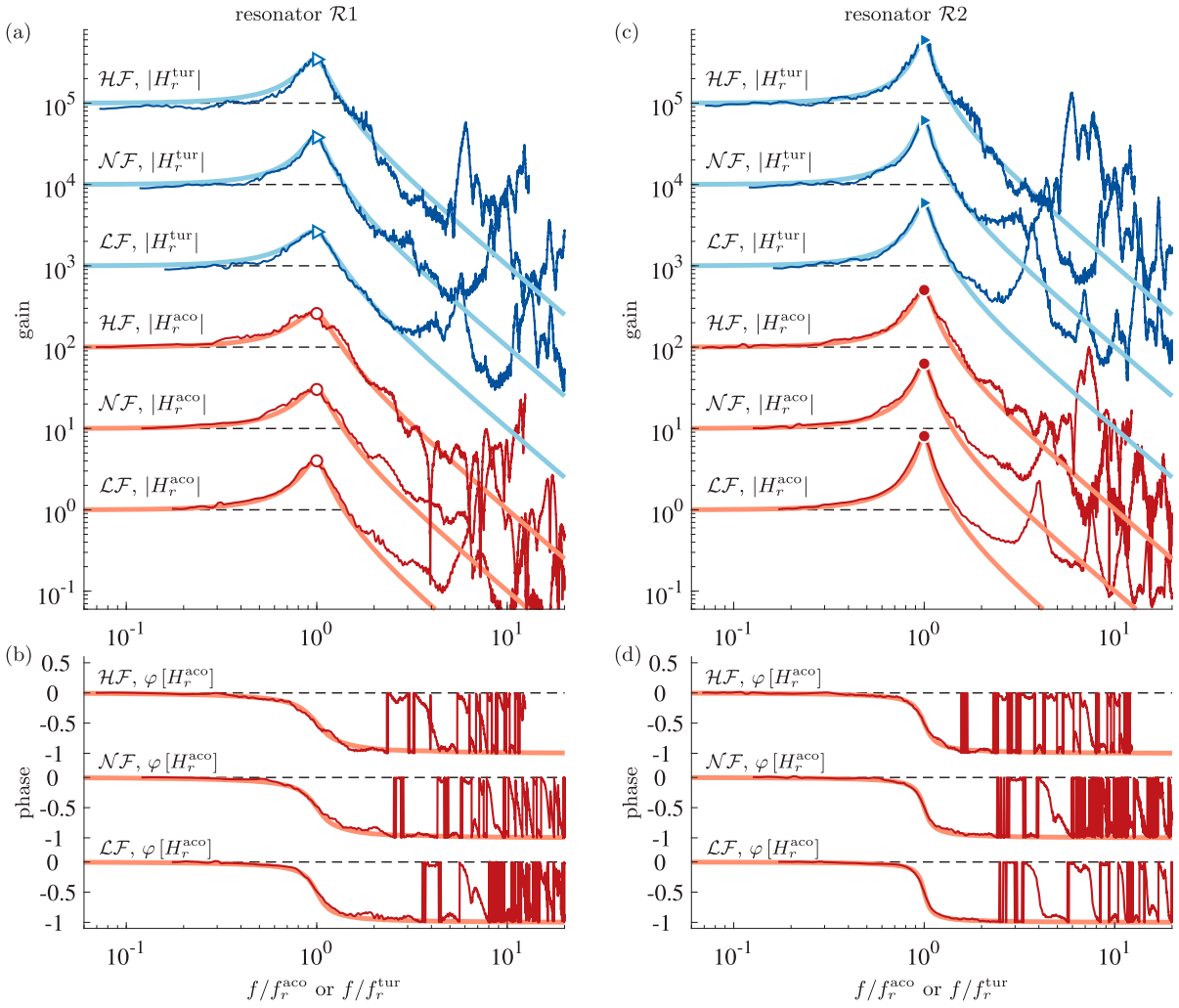

Figure 5. (a,b) For resonator $\mathcal{R}1$, bode plots of H_r^{aco} with the gain in sub-figure (a) and the phase in sub-figure (b), for the $\mathcal{LF}$, $\mathcal{NF}$, and $\mathcal{HF}$ cases (series or redred lines). In addition, the gain of $|H_r^{\mathrm{tur}}|$ is shown in sub-figure (a) with the series of blueblue lines. Each gain approaches unity for low frequencies, but for clarity of visualisation, gain curves are offset sequentially (except for the bottom one) in the ordinate coordinate by steps of one decade. Experimental data is always shown with a dark line, while a fit of the 2nd-order model transfer kernel is shown with a thick light-shaded line. (c,d) Similar to sub-figures (a,b), but now for resonator $\mathcal{R}2$.

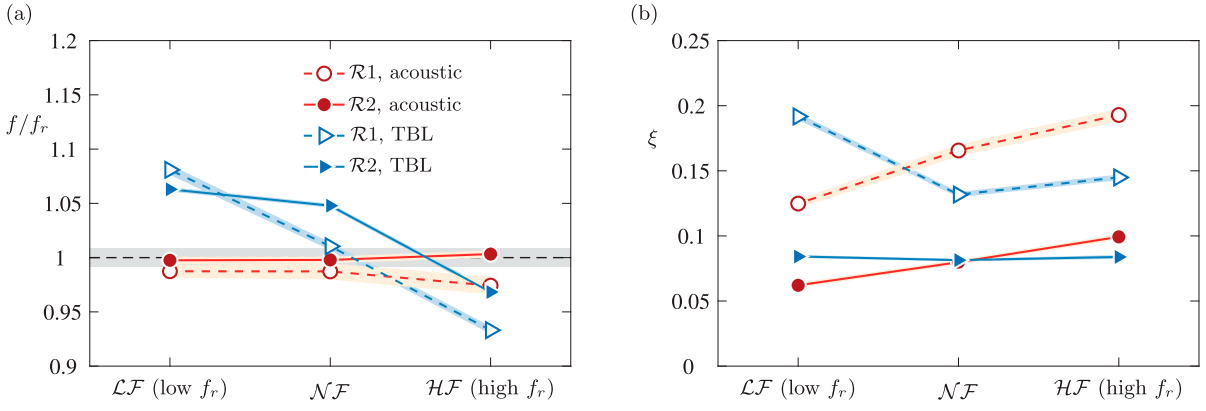

Figure 6. (a) Empirically determined resonance frequencies in the case of acoustic excitation (f_r^{aco}) and excitation by the grazing TBL flow (f_r^{tur}), normalised with the design resonance frequency listed in Table 2 (f_r), for the $\mathcal{LF}$, $\mathcal{NF}$, and $\mathcal{HF}$ cases and for both resonators $\mathcal{R}1$ and $\mathcal{R}2$. Similar to sub-figure (a), but now for the damping constant ξ.

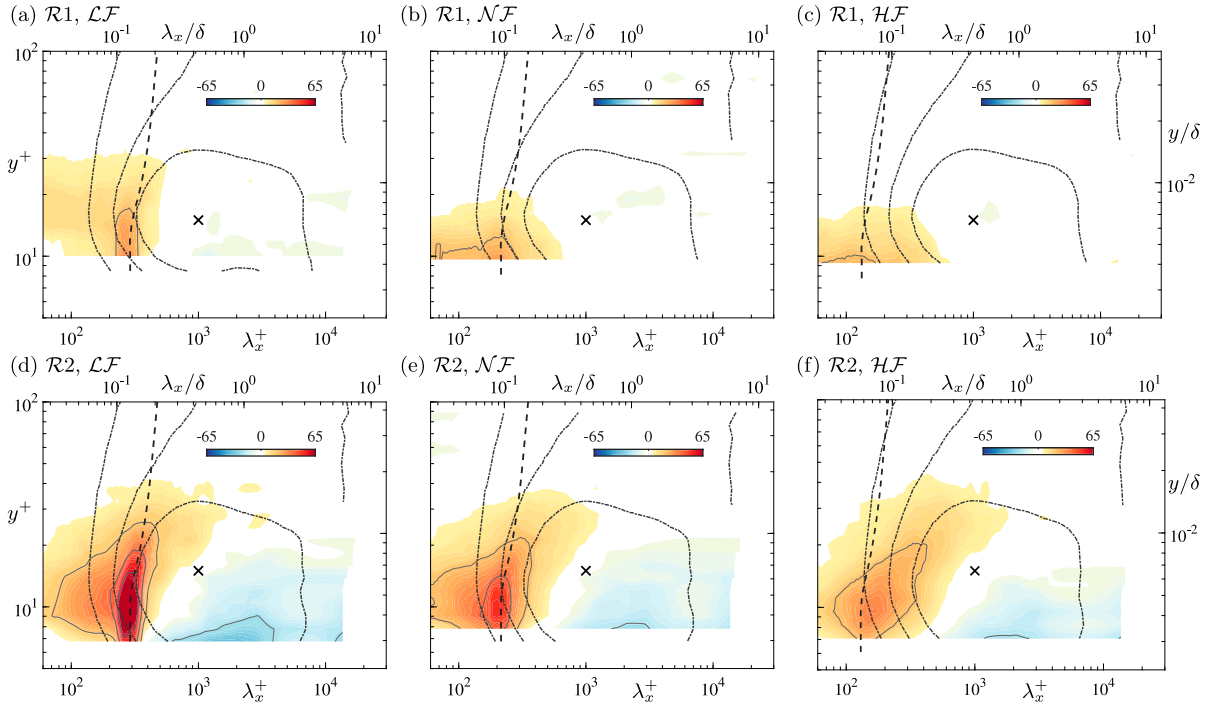

Figure 7. Filled contours of the percentage difference of the premultiplied energy spectrograms $k_x^+\phi_{uu}^+$, for resonators $\mathcal{R}1$ (a–c) and $\mathcal{R}2$ (d–f) for all three resonance cases, at $x^+ \approx 186$, relative to the baseline spectrogram of the unperturbed flow. Negative values (blueblue) indicate an energy reduction due to the presence of the HR, while positive values (redred) indicate an energy intensification. Dark grey solid iso-contours correspond to levels of ±20%, ±40%, and ±60%. A black dashed line corresponds to the constant resonance frequency; note that $\lambda_x = \overline{U}_c(y)/f$. Dash-dotted lines indicate three iso-contours of the absolute value of the baseline spectrogram, $k_x^+\phi_{uu}^+ = 0.4$, 0.8 and 1.2, to highlight where changes in the energy are relevant in terms of underlying energy in the flow.

5. Flow response of the turbulent boundary layer

5.1. Statistical energy response of the turbulent boundary layer

In order to inspect how the HR affects the grazing TBL flow, we first consider the change in the streamwise energy spectra inferred from the HWA data. For resonator $\mathcal{R}1$, changes in the premultiplied energy spectrogram at $x^+ \approx 186$ are shown in Figure 7(a–c), for all three resonance cases. Changes are presented in terms of a percentage difference, relative to the spectrogram of the baseline flow. In order to assess whether percentage-differences occur in parts of the (λ_x, y) space where a significant fraction of the streamwise TKE resides, three iso-contours of the baseline spectrogram are superimposed (dash-dotted lines), corresponding to $k_x^+\phi_{uu}^+ = [0.4; 0.8; 1.2]$, together with a cross-marker indicating the location of the inner-spectral peak at $(\lambda_x^+, y^+) = (1000, 15)$. Note that energy-differences were computed in the frequency domain, after which the spatial wavelength is taken as $\lambda_x \equiv \overline{U}_c(y)/f$ with $\overline{U}_c(y)$ being the local mean velocity. Nevertheless, because there is no apparent difference in the mean velocity profiles of the baseline flow and the different resonance cases (see Figure 8(a)), a major flow acceleration/deceleration is absent and spatial wavelengths remain reflective of the typical values found in nominal, equilibrium TBL flows.

When inspecting the change in streamwise TKE, an increase is observed surrounding the resonance scale, which appears to be strongest in the $\mathcal{LF}$ case. An increase of more than 20% is observed in the buffer region (Figure 7(a)), but the effect is only confined to $y^+ \lesssim 30$. For higher resonance frequencies (smaller scales), the increase in energy weakens as it becomes less narrow-band around the resonance scale. Changes in the streamwise TKE due to the presence of resonator $\mathcal{R}2$ are larger compared to resonator $\mathcal{R}1$, as seen in Figure 7(d–f). General observations are similar in that the largest increase of energy (up to 70%) appears at the resonance scale for the $\mathcal{LF}$ case and this weakens when moving from the $\mathcal{LF}$ to $\mathcal{HF}$ case. A stronger effect induced by resonator $\mathcal{R}2$, in comparison to resonator $\mathcal{R}1$, is consistent with the lower damping constants (Figure 6(b)).

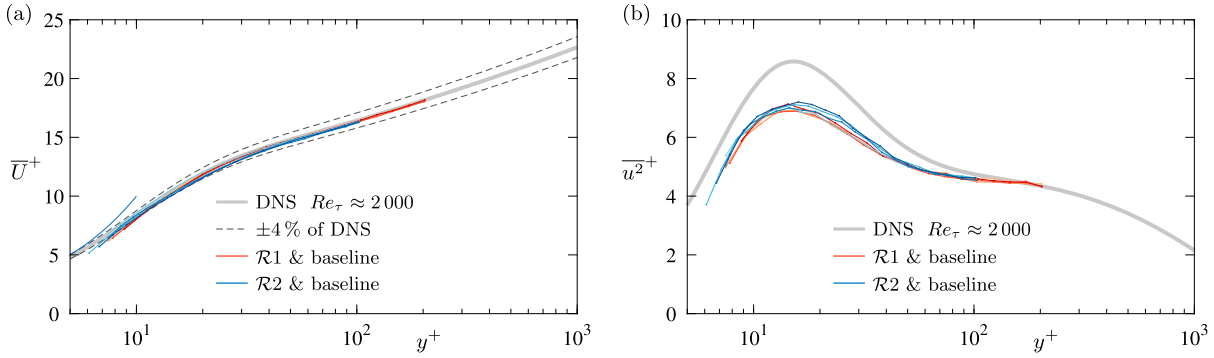

Figure 8. (a) Streamwise MVP at $x^+ \approx 186$, corresponding to the data shown in Figure 7. The bundle of red profiles correspond to resonator $\mathcal{R}1$, with the four lines of increasing colour intensity corresponding to the baseline flow, $\mathcal{HF}$ case, $\mathcal{NF}$ case, and $\mathcal{LF}$ case, respectively; the bundle of blue profiles is similar to the red ones, but now for $\mathcal{R}2$. MVP's are compared to DNS data of turbulent channel flow at $Re_\tau \approx 2000$ [6]. (b) Similar to sub-figure (a), but now for the streamwise TKE profiles (data are not corrected for spatial resolution effects and all profiles are therefore attenuated in comparison to the DNS profile as discussed in § 2.2).

Still, the energy change is confined to the buffer region $y^+ \lesssim 30$ and no disturbances penetrate the logarithmic region.

A major difference between resonators $\mathcal{R}1$ and $\mathcal{R}2$ is that, for the $\mathcal{R}2$ resonators, a strong attenuation of low-frequency energy is observed. More than 20% of attenuation is present in the case of $\mathcal{LF}$, at scales on the order of the boundary layer thickness, e.g. $\lambda_x^+ = 2280$ (Figure 7(d)). In § 5.3 we hypothesise a mechanism for this decrease in energy, after inferring the resonator's response behaviour under grazing flow from the velocity field data. Finally, it is worth noting that the low-frequency energy attenuation, and energy intensification of resonance-scales, results in a nearly zero-net energy change of the resolved TKE at this location of $x^+ \approx 186$: profiles of the resolved TKE collapse in Figure 8(b). Though, this net-change is expected to be dependent on the spatial location. And so, the acquisition of spatial-temporal data is required to analyse the spatial-spectral trends of the energy changes (e.g. obtained by way of time-resolved PIV), which is reserved for future work.

5.2. Conditionally-averaged response of the turbulent boundary layer

Given that $\mathcal{R}2$ yielded more pronounced changes in the streamwise spectra (in comparison to $\mathcal{R}1$) – presumably due to the lower damping constants (friction losses in the orifice) – we here proceed with results of $\mathcal{R}2$ only. First, pressure time series of p_c are shown in Figure 9 for all three resonance frequencies, and for a time span of 10 resonance periods. Raw time series are shown with the grey thick lines. Signals are not perfectly harmonic with resonance period $T_r = 1/f_r$, given that the wall-pressure excitation is broadband. Still, resonance dominates since f_r roughly coincides with the dominant energetic frequencies of the wall-pressure spectrum. Intensity of the pressure fluctuations in the cavity, at resonance, are related to the excitation amplitude and gain factor. The root-mean-square (rms) of the wall-pressure fluctuations beneath the undisturbed TBL flow is $p^+_{w,\mathrm{rms}} \approx 3.31$ (following the empirical trend of Klewicki et al. [72] and a previous study in the same facility [61]). The cavity pressure-rms is roughly 5.4 times higher for the $\mathcal{LF}$ case, and closely resembles the gain factor at resonance ($0.5/\xi^{\mathrm{tur}} \approx 5.9$ from Figure 5(c)). In the remainder of this section we analyse the strength by which such a gained cavity-pressure feeds a disturbance back in the grazing TBL flow.

With the aid of the synchronised data of the cavity pressure, p_c, and the u velocity from HWA, a conditional average of the velocity fluctuations is generated. At first, raw time series are filtered with a narrow bandpass kernel around the resonance frequency, $f \in [0.75f_r^{\mathrm{tur}},\ 1.50f_r^{\mathrm{tur}}]$ to yield p_{cF}, shown with the black lines in Figure 9. This filtering is performed to accurately identify local maxima associated to the resonance period. The peak-detection algorithm only retains maxima of which the amplitudes in both the filtered and raw time series exceed $0.5p^+_{cF,\mathrm{rms}}$ (this threshold is shown with the blue dashed lines). Results are insensitive to the bounds chosen for the bandpass kernel and the amplitude-threshold, since only the magnitude of the conditional average is affected, not the relative difference between cases; neither the conclusions. Time series of u are conditionally-averaged to the total number of N_m local maxima occurring at τ_i with $i = 1 \ldots N_m$, at

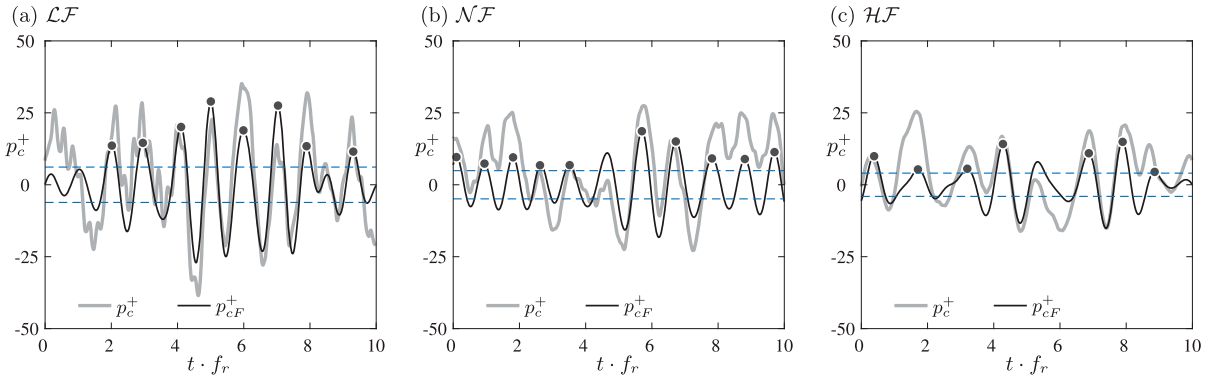

Figure 9. Time series of the inner-normalised cavity pressure corresponding to $\mathcal{R}2$, for the (a) $\mathcal{LF}$ case, (b) $\mathcal{NF}$ case, and (c) $\mathcal{HF}$ case. Raw measurements are shown with the grey thick line, while a filtered version with a bandpass of $f \in [0.75f_r^{\text{tur}}, 1.50f_r^{\text{tur}}]$ is shown with the black line. Blue dashed lines indicate $\pm 0.5 p^+_{cF,\text{rms}}$.

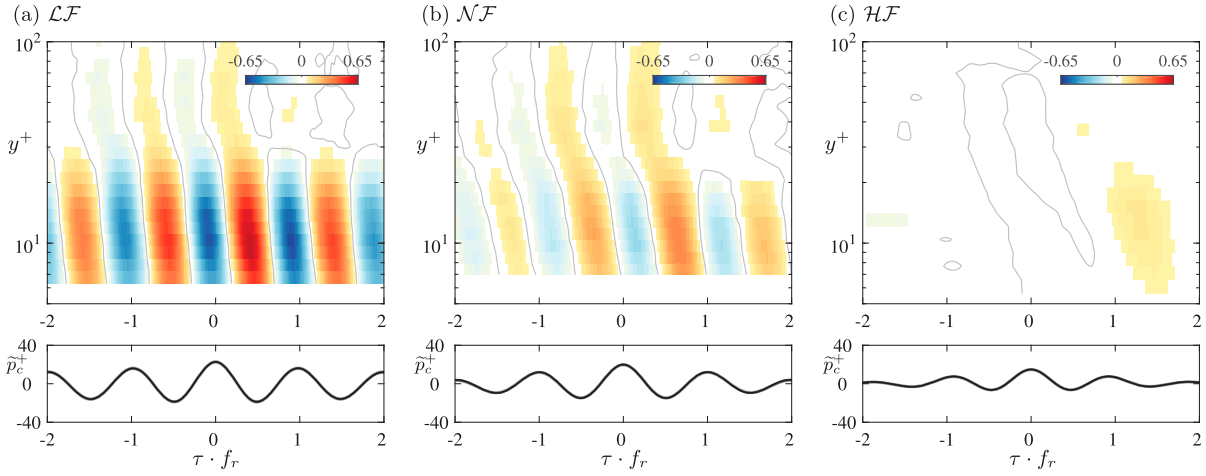

Figure 10. Iso-contours of the conditionally-averaged streamwise velocity fluctuations, $\widetilde{u}^+(y, \tau)$, inferred from the HWA data at $x^+ \approx 186$, for the (a) $\mathcal{LF}$ case, (b) $\mathcal{NF}$ case, and (c) $\mathcal{HF}$ case. Fluctuations are conditioned on the local maxima of the band-pass filtered cavity pressure signals (illustrated in Figure 9); conditional averages of the (raw) cavity pressure signals themselves are shown in the bottom plots.

each y position, according to:

$$\widetilde{u}\left(y, \tau\right) = \frac{1}{N_m} \sum_{i=1}^{N_m} u\left(y, t - \tau_i\right). \tag{5}$$

Where N_m is the number of maxima identified, τ being the time coordinate of the conditional average, with $\tau = 0$ signifying the conditioning point. Figure 10 presents iso-contours of $\widetilde{u}(y, \tau)$ for a time span of 4 resonance periods, alongside the conditional average of the unfiltered cavity pressure, $\widetilde{p}_c$. Cavity-pressure coherent u fluctuations are strongest in the $\mathcal{LF}$ case and is consistent with the spectrograms in Figure 7. When moving towards the $\mathcal{HF}$ case, the magnitude decreases due to the lower level of pressure oscillations in the cavity. Moreover, the conditional average of the cavity pressure for the $\mathcal{HF}$ case displays a decaying amplitude away from $\tau = 0$, because the pressure is more broadband and the phase of resonance varies more erratically with time (recall Figure 9(c)) in comparison to the $\mathcal{NF}$ or $\mathcal{LF}$ cases. This is also related to less gain in the $\mathcal{HF}$ case (recall a higher ξ) and thus the magnitude of pressure resonance-oscillations is lower compared to the broadband content. Finally, the inclination of the velocity perturbations suggests that they are convective in nature and adapt to the mean shear in the TBL flow at the position of the measurement (a perturbation is first observed at positions further away from the wall, at $x^+ \approx 186$).

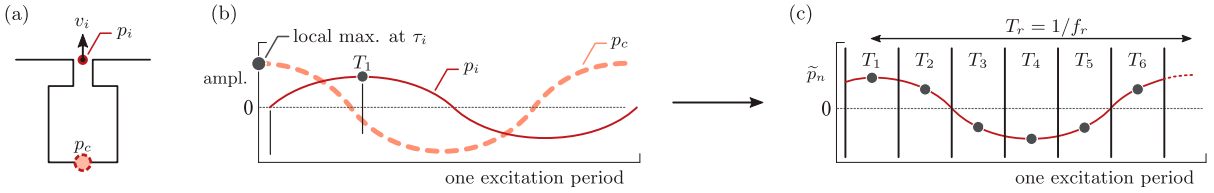

Figure 11. Illustration of the bins used for conditional averaging of the PIV velocity fields. (a) Locations of the neck-inlet and cavity pressures, and (b) the phase-offset between the signals with the local maximum in p_c at time instant τ_i, and the central time instant T_1 of the first bin. (c) All six central time instants in relation to the conditionally-averaged, periodic neck-inlet pressure.

Conditional averages of the 4000 PIV-based velocity fields – available for each resonator case – to the periodic resonance cycle, allow for a detailed inspection of the spatio-temporal evolution of the convective perturbations. Local maxima in the cavity pressure (Figure 9) occur at time instances denoted as τ_i and are identical to the ones used in conditional averaging the hot-wire time series. The resonance period T_r is now divided into six equal-duration bins, each of which is centred at T_i, with $i = 1 \ldots 6$. Given the synchronised acquisition of the laser Q-switch signal of the first pulse of the PIV image pair together with the cavity pressure data, each PIV-based velocity field is assigned to one of the 6 bins. It must be noted that bin 1 (and thus also the subsequent bins) is offset from the time instance of the local maxima in the cavity pressure signal, to account for two factors:

(1) For resonators with slender cavities of length L, a relatively small value of λ_a/L (λ_a is the acoustic wavelength at resonance) causes a temporal lag between the pressure at the cavity bottom (where it is measured, see Figure 3(d)) and the pressure in the near-vicinity of the orifice. As such, time instants τ_i are offset by L/a_0, forward in time, so that conditional averaging is done in relation to the pressure at the top of the cavity. This offset is minor in the current work: the $\mathcal{LF}$ case of $\mathcal{R}2$ has the deepest cavity with $\lambda_a/L \approx 7.4$ (Table 2) and this results in an offset of $L/a_0 = L/(a_0/f_r)T_r \approx 0.14T_r$.
(2) Given the 0.5π phase offset between the cavity pressure and the neck-inlet pressure at resonance, time instants of local maxima in the cavity pressure, τ_i, are offset by $\frac{1}{4}T_r$, also forward in time. This ensures that conditional averaging is done on a signal that is representative of the neck-inlet pressure (see Figure 2(d)).

In short, the central time instant of bin 1 corresponds to $T_1 = \tau_i + L/a_0 + 0.25T_r$ and signifies the maximum resonance pressure at the neck-inlet (recall that τ_i corresponds to the maximum resonance pressure at the cavity-bottom). The conditionally-averaged pressure signal at the neck-inlet is denoted as $\widetilde{p}_n$ and is illustrated in Figure 11, together with the central time instants of all 6 bins. For determining the local maxima in the cavity pressure, a threshold was implemented to omit 'weak resonance' periods. As such, for the $\mathcal{LF}$ case as an example, 3112 fields of the in total 4000 PIV fields were used for conditional averaging and were divided nearly equally over all six bins (484 fields for the bin with the lowest number of fields). Prior to averaging the velocity fields corresponding to each bin, a singular value decomposition (SVD) of the statistically-independent $u(x, y, t_i)$ and $v(x, y, t_i)$ snapshots was conducted in a combined $[u; v]$ fashion. Each field at t_i was then regenerated through a low-dimensional reconstruction with a subset of the in total 3112 modes (the subset comprised modes $m = 1 \ldots M$, where $M = 50$ was determined so that 40% of the total-resolved-TKE was reconstructed). So while this step is not required, it accelerated the convergence of the conditional averages. It was also confirmed that this step did not remove any fluctuations that are phase-consistent with the resonance cycle, since these were relatively energetic and part of modes 1 to M (the choice of retaining 40% of the total-resolved-TKE was confirmed not to affect the conclusions made).

Conditionally-averaged velocity fields for the $\mathcal{LF}$ case are shown in Figure 12(a) (contour of streamwise velocity $\widetilde{u}$) and Figure 12(b) (contour of wall-normal velocity $\widetilde{v}$). Fields are shown for each T_i, $i = 1 \ldots 6$, and vectors are superimposed on each field (with a vector skip of 2). Only a domain up to a wall-normal distance of $y^+ \approx 100$ is considered, given that our previous analysis already indicated a relatively limited wall-normal region influenced by the resonator. In streamwise direction, a total length of $\Delta x^+ \approx 750$ is considered and

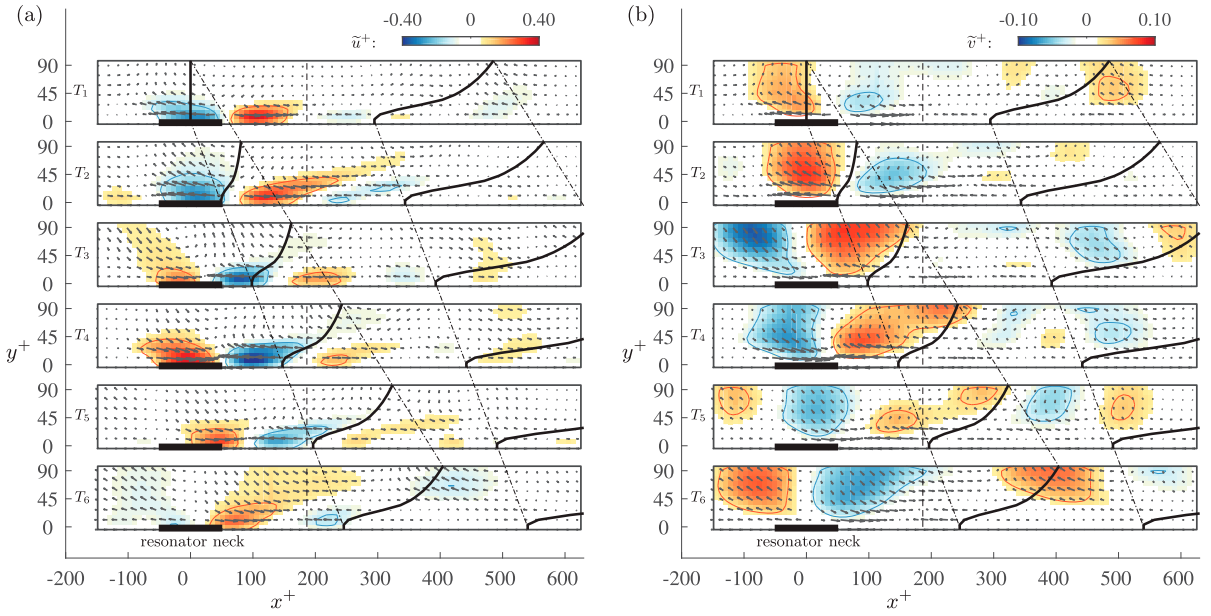

Figure 12. Iso-contours of the conditionally-averaged (a) streamwise, $\widetilde{u}(x, y, T_i)$, and (b) wall-normal velocity fluctuations, $\widetilde{v}(x, y, T_i)$, for the $\mathcal{LF}$ case of $\mathcal{R}2$. Velocity fields are shown for all 6 instances, T_i with $i = 1 \ldots 6$, corresponding to the six central instants of each bin used for conditional averaging over one period, T_r (see Figure 11). The resonator neck of $d^+ = 102$ is indicated with the thick black line; a vertical line at $x^+ = 186$ indicates the hot-wire profile. A vertical line above the resonator in the T_1 field is displaced in each subsequent field according to the mean convection velocity profile, $\overline{U}_c(y)$, as described in the text. Because of periodicity in the conditional average, the visualisation continues in frame T_1 after frame T_6.

includes the resonator neck of which the extent is indicated with the thick line of length $d^+ = 102$. To ease the inspection of the convecting flow field during the resonance cycle, a vertical line above the resonator (in the field at T_1) is displaced in each subsequent field according to the mean convection velocity profile $\overline{U}_c(y)$ (taken as the local mean velocity profile), except for $y^+ \lesssim 10$, where the convection velocity plateaus to a constant value of $\overline{U}_c^+ = 10$. Given the periodicity of the conditional average, this line continues to deform when moving from T_6 to T_1 and beyond.

Vertical velocity fluctuations $\widetilde{v}$ in Figure 12(b) show an apparent outflow and inflow phase. These regions of positive and negative vertical velocity are accompanied by negative and positive streamwise velocity fluctuations $\widetilde{u}$, respectively (see Figure 12(a)). This indicates that the flow features associated with resonance are similar to the ones induced by zero-mass net flux jetting: during the inflow phase the high-momentum fluid in the TBL flow is pulled towards the wall, and vice versa during the outflow phase.

Before proceeding with flow-field observations, the conditionally-averaged fields for the two remaining resonance cases ($\mathcal{NF}$ and $\mathcal{HF}$) are presented in Figures 13 and 14, and are shown in an identical format as the one of the $\mathcal{LF}$ case in Figure 12. For the $\mathcal{LF}$ case, the velocity disturbance of the resonator persists downstream for a duration of roughly one resonance cycle. This is generally true for the $\mathcal{NF}$ case also, although the $\widetilde{u}$ motions are slightly weakened while the $\widetilde{v}$ ones contain a more coherent character and persist downstream for almost two resonance cycles. This is ascribed to the fact that for the $\mathcal{NF}$ case the resonator cycle is tuned to the period of the most energetic, naturally-occurring v motions. That is, for the $\mathcal{NF}$ case, $\lambda_{x,r}^+ \approx 231$ (Table 2) resides closest to the inner-spectral peak of v at $(\lambda_x^+, y^+) \approx (250, 100)$. To understand the significant weakening of the $\widetilde{u}$ (and $\widetilde{v}$) motions in the $\mathcal{HF}$ case, we consider the convective nature of the perturbations. For this, a stroke ratio is defined with two time scales: (1) the half-period of resonance, $t_r \equiv T_r/2$, that is characteristic of the outflow and inflow duration, and (2) the convective time of the flow past the resonator's neck, $t_c \equiv d/\overline{U}_c$, with $\overline{U}_c^+ = 10$, yielding

$$\mathrm{SR} \equiv \frac{t_r}{t_c} = \frac{\overline{U}_c T_r}{2d}. \tag{6}$$

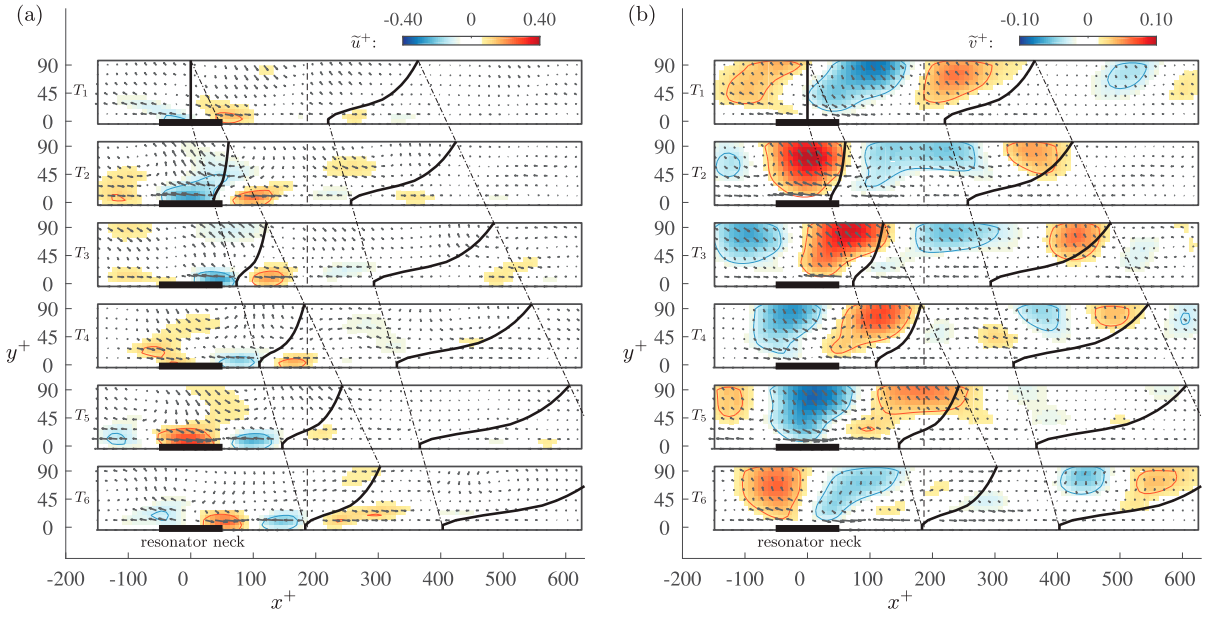

Figure 13. Similar to Figure 12, but now for the $\mathcal{NF}$ case.

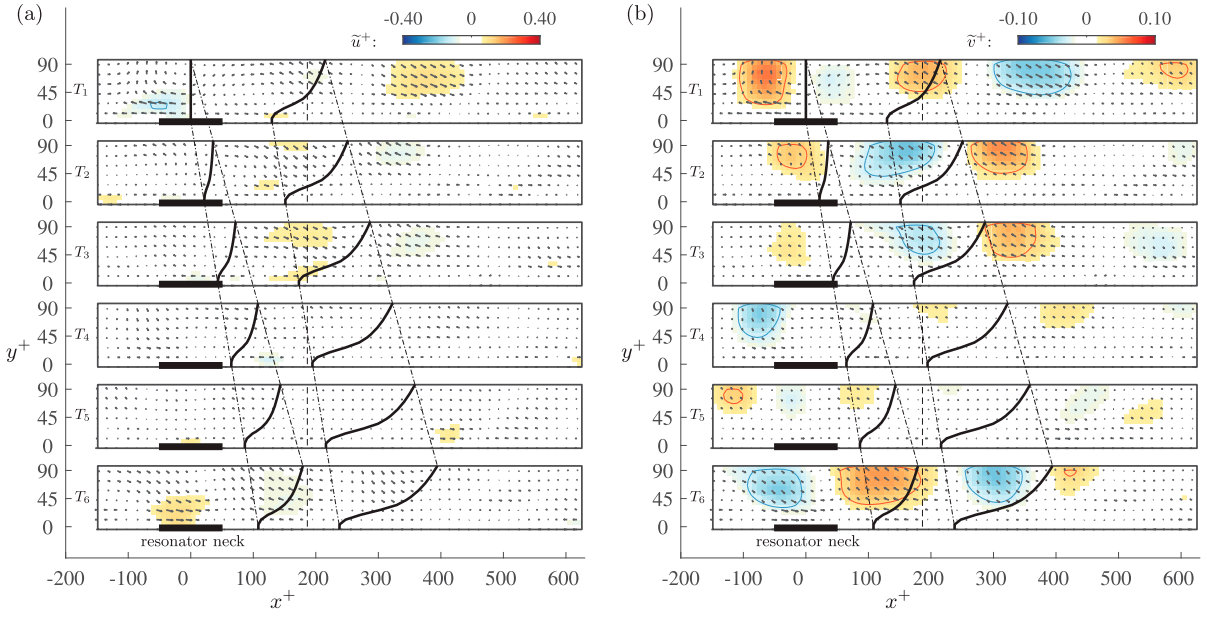

Figure 14. Similar to Figure 12, but now for the $\mathcal{HF}$ case.

For resonator $\mathcal{R}2$, SR $\approx$ 1.45 for the $\mathcal{LF}$ case, SR $\approx$ 1.08 for the $\mathcal{NF}$ case and SR $\approx$ 0.64 for the $\mathcal{HF}$ case. When SR $>$ 1, outflow and inflow phases are fully established throughout the entire neck orifice, e.g. an inflow signature associated with increased streamwise velocity convects over the entire orifice before it reverses to the outflow phase. When SR $<$ 1 (in the $\mathcal{HF}$ case), an outflow and/or inflow phase does not convect past the orifice before the neck-inlet velocity changes sign. This reduces the effective diameter of the neck: i.e. near the neck's trailing-edge signatures of the outflow and inflow phases are weakened as they are, on average, opposing one another.

5.3. Pressure-velocity coupling at the neck-inlet

When time-resolved pressure information is available at the neck-inlet, together with time-resolved velocity fields, the local wall-impedance at the neck-inlet, $Z_i \in \mathcal{C}$ (as discussed in § 1.2), could be inferred from the

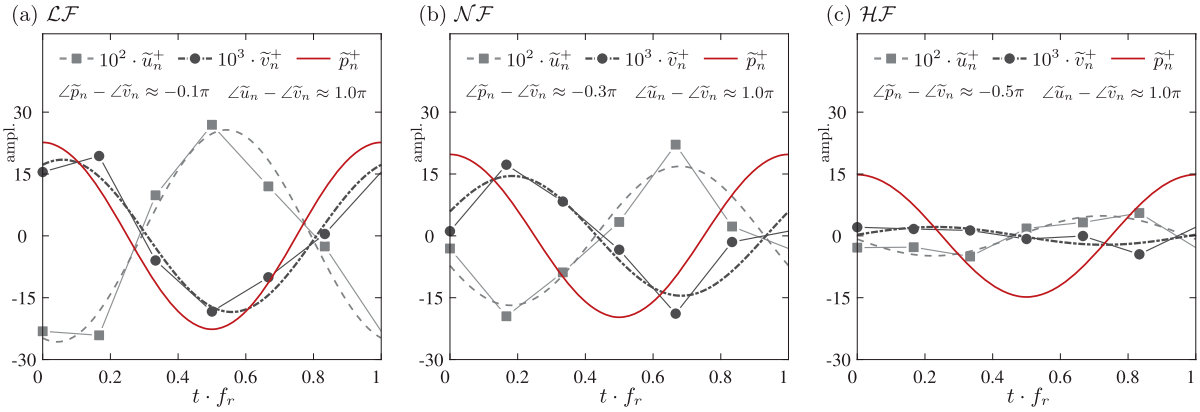

Figure 15. Conditionally-averaged streamwise velocity, wall-normal velocity and pressure fluctuations over the orifice of $\mathcal{R}2$, for the (a) $\mathcal{LF}$ case, (b) $\mathcal{NF}$ case, and (c) $\mathcal{HF}$ case. For each of the 6 instances in the resonance cycle (corresponding to the fields shown in Figures 12,13 and 14) the velocity fluctuations are averaged over a thin region above the orifice ($y^+ \approx 7$ and $x \in [-0.4d, 0.4d]$) and shown with the markers; harmonic fits to the data are shown with the dashed and dash-dotted lines. A harmonic pressure oscillation reflects the pressure at the neck-inlet, inferred from the conditionally-averaged cavity pressure with the proper phase shifts applied (described in the text).

data. However, given the absence of time-resolved data, an attempt is made to infer the impedance relation at the resonance scale only ($f = f_r$) from the conditionally-averaged behaviour. The average streamwise and vertical velocities are extracted just above the neck-inlet at $y^+ \approx 7$, from the conditionally-averaged velocity fields (thus from the fields presented in Figure 12(a,b)). These velocities are denoted as $\widetilde{u}_n$ and $\widetilde{v}_n$ and are plotted in Figure 15(a) for each of the 6 instances in the resonance cycle of the $\mathcal{LF}$ case; harmonic waves are fitted to the discrete data points and are described in the caption. In addition, a time series of the neck-inlet pressure is superimposed following the discussion of Figure 11, in which it was pointed out that the velocities are conditionally-averaged so that the first bin of the resonance cycle corresponds to the maximum pressure at the neck-inlet. Figure 15(b,c) are similar to Figure 15(a), but correspond to the $\mathcal{NF}$ and $\mathcal{HF}$ cases, respectively.

Only the phase relation between $\widetilde{u}_n$, $\widetilde{v}_n$ and $\widetilde{p}_n$ can be interpreted, while their amplitude ratios (e.g. the ratio of the maximum in $\widetilde{p}_n$ to the maximum in $\widetilde{v}_n$ for determining $|Z(f \equiv f_r)|$) are non-physical given that velocities and pressure are based on conditional averaging, and the pressure magnitude is representative of the cavity pressure. Nevertheless, phase relations reveal that:

(1) Vertical and horizontal velocities appear in perfect phase opposition: the phase shifts between the harmonic functions fitted to the data are 1.0π for all three resonance cases. This is direct evidence that at resonance, the near-wall horizontal velocity in the sheared TBL flow reacts instantly to the vertical perturbations displacing pockets of air with high-/low-speed streamwise velocity.
(2) For the $\mathcal{LF}$ case, the vertical velocity $\widetilde{v}_n$ and neck-inlet pressure are nearly in-phase with only a 0.1π phase shift. For an acoustic resonator at resonance, this in-phase behaviour is expected (recall Figure 2(b,d); $\varphi[Z_i^*] = 0$ at $f = f_r$). When moving towards the other resonance cases, this phase drifts towards a half-out-of-phase behaviour for the $\mathcal{HF}$ case: pressure is leading the vertical velocity, which would reflect sub-resonance behaviour as illustrated in Figure 2(b,e). We conjecture that this drift in the phase relation, going from the $\mathcal{LF}$ case to the $\mathcal{NF}$ case and the $\mathcal{HF}$case, is due to a response delay in the vertical velocity caused by a significant part of the vertical perturbation being attenuated near the trailing-edge of the neck due to the decreasing stroke ratio, SR.

Finally, the attenuation of large-scale energy that was discussed in § 5 with the aid of Figure 7, is commented on here. Previously it was shown that this large-scale attenuation is strongest for the $\mathcal{LF}$ case; in addition, it was confirmed that the HR behaves in a classical sense, following Figure 2 (at least for the resonance frequency that was analysed in a conditional sense from the non-time-resolved PIV velocity fields). When now concentrating on the low-frequency fluctuations for the $\mathcal{LF}$ case, we presume that the large-scale

fluctuations in the neck-inlet pressure of the resonator couple to the one of the incoming flow. Then, vertical velocity fluctuations induced by the resonator's impedance condition are *lagging* the incoming, grazing velocity fluctuations (a case in between Figure 2(c,d)). Consequently, a larger percentage of the low frequency velocity fluctuations in the TBL flow are opposed than that they are enhanced. However, time-resolved spatial velocity measurements, synchronised with neck-pressure information, must be conducted to confirm this claim and to expose the exact mechanism by which near-wall large-scale u fluctuations are attenuated.

6. Concluding remarks

This work considered single, miniature HRs beneath grazing TBL flow. Response details of the resonator itself, as well as the resonator-induced changes to the grazing TBL flow dynamics were investigated with a particular focus of tuning the resonator to the spatio-temporal characteristics of the most intense near-wall vertical velocity and wall-pressure fluctuations. Investigations of two neck-orifice diameters of $d^+ = 68$ and $d^+ = 102$, both with three resonance frequencies relating to a spatial scale of $\lambda_x^+ \equiv U_c^+/f^+ \approx 250$ (the inner-spectral peak of v and p_w) and sub- and super-wavelength scaling tuned to $\lambda_x^+ \approx 126$ (-46%) and $\lambda_x^+ \approx 313$ ($+35\%$), respectively, yielded several conclusions:

(1) All HRs beneath the grazing flow behave acoustically: resonance frequencies were relatively well-predicted to within $\pm 10\%$, through classical expressions of acoustic resonators with end-corrections;
(2) The smaller resonator with $d^+ = 68$ experienced much larger frictional losses (damping coefficient roughly 75% to 100% larger), so that its effect on the grazing TBL flow was minor: particularly in the large-scale range of turbulence scales where a negligible difference was observed, while the larger resonator with $d^+ = 102$ resulted in an energy attenuation;
(3) For the larger neck diameter of $d^+ = 102$, non-time resolved PIV-based velocity fields revealed that near-wall velocity fluctuations in v, reaching beyond $y^+ \approx 100$, are coupled to the resonance cycle; u fluctuations also manifest this coupling and are, as expected, in phase opposition with the v fluctuations;
(4) Persistence of the perturbations of the resonance-scale downstream of the resonator was rather limited: in all resonance cases the effects were not coherent beyond a convective distance of two resonance periods;
(5) Spectral analyses of time-resolved hot-wire data (along a wall-normal profile $135l^*$ downstream of the neck-trailing edge) revealed that, in the near-wall region, large-scale energy (at a temporal frequency roughly one decade smaller than the resonance frequency) was attenuated by over 20%.
(6) Conditional averaging of the non-time resolved velocity fields, to the resonance cycle of the cavity pressure, exposed that at resonance the low-frequency resonator comprised a phase relation between the vertical velocity at the neck-inlet, and the co-existing pressure, according to a classical resonator at resonance (in-phase behaviour). A drift in this phase relation was observed for the higher-frequency resonator, which is ascribed to an effective smaller diameter when the stroke ratio becomes smaller than unity.

Our current research findings benefit the future development of passive surfaces with distributed resonators. Such surfaces will manipulate the energy content of the grazing wall-bounded turbulence, and are of interest for investigating their effect on the mean skin friction generation mechanisms (and thus for investigating their ability to be utilised as boundary-layer flow control surfaces).

Acknowledgments

We wish to acknowledge Stefan Bernardy, Peter Duyndam and Frits Donker Duyvis for technical assistance during the experimental campaign.

Disclosure statement

No potential conflict of interest was reported by the author(s).

Funding

Financial support of the European Office of Aerospace Research & Development (EOARD) of the U.S. Air Force Office of Scientific Research (AFOSR) under Award No. FA8655-22-1-7168 (Intnl. Program Officer Dr. Douglas Smith & Program Officer Dr. Gregg Abate) is gratefully acknowledged.

References

[1] Hwang Y. Near-wall turbulent fluctuations in the absence of wide outer motions. J Fluid Mech. 2013;723:264–288. doi: 10.1017/jfm.2013.133
[2] Kline SJ, Reynolds WC, Schraub FA, et al. The structure of turbulent boundary layers. J Fluid Mech. 1967;30:741–773. doi: 10.1017/S0022112067001740
[3] Robinson SK. Coherent motions in turbulent boundary layers. Annu Rev Fluid Mech. 1991;23:601–639. doi: 10.1146/fluid.1991.23.issue-1
[4] Wallace JM, Eckelmann H, Brodkey RS. The wall region in turbulent shear flow. J Fluid Mech. 1972;54:39–48. doi: 10.1017/S0022112072000515
[5] Mathis R, Hutchins N, Marusic I. Large-scale amplitude modulation of the small-scale structures in turbulent boundary layers. J Fluid Mech. 2009;628:311–337. doi: 10.1017/S0022112009006946
[6] Lee M, Moser RD. Direct numerical simulation of turbulent channel flow up to $Re_\tau = 5200$. J Fluid Mech. 2015;774:395–415. doi: 10.1017/jfm.2015.268
[7] Panton RL, Lee M, Moser RD. Correlation of pressure fluctuations in turbulent wall layers. Phys Rev Fluids. 2017;2:Article ID 094604. doi: 10.1103/PhysRevFluids.2.094604
[8] Lee M, Moser RD. Spectral analysis of the budget equation in turbulent channel flows at high Reynolds number. J Fluid Mech. 2019;860:886–938. doi: 10.1017/jfm.2018.903
[9] Tsuji Y, Fransson JHM, Alfredsson PH, et al. Pressure statistics and their scaling in high-Reynolds-number turbulent boundary layers. J Fluid Mech. 2007;585:1–40. doi: 10.1017/S0022112007006076
[10] Blackwelder RF, Eckelmann H. Streamwise vortices associated with the bursting phenomenon. J Fluid Mech. 1979;94:577–594. doi: 10.1017/S0022112079001191
[11] Offen GR, Kline SJ. A proposed model of the bursting process in turbulent boundary layers. J Fluid Mech. 1975;70:209–228. doi: 10.1017/S002211207500198X
[12] Fukagata K, Iwamoto K, Kasagi N. Contribution of Reynolds stress distribution to the skin friction in wall-bounded flows. Phys Fluids. 2002;14(11):L73–L76. doi: 10.1063/1.1516779
[13] Jiménez J, Pinelli A. The autonomous cycle of near-wall turbulence. J Fluid Mech. 1999;389:335–359. doi: 10.1017/S0022112099005066
[14] Orlandi P, Jiménez J. On the generation of turbulent wall friction. Phys Fluids. 1993;6(2):634–641. doi: 10.1063/1.868303
[15] Adrian RJ, Meinhart CD, Tomkins CD. Vortex organization in the outer region of the turbulent boundary layer. J Fluid Mech. 2000;422:1–54. doi: 10.1017/S0022112000001580
[16] Hutchins N, Marusic I. Large-scale influences in near-wall turbulence. Philos Trans R Soc A. 2007;365:647–664. doi: 10.1098/rsta.2006.1942
[17] Marusic I, Baars WJ, Hutchins N. Scaling of the streamwise turbulence intensity in the context of inner-outer interactions in wall-turbulence. Phys Rev Fluids. 2017;2:Article ID 100502. doi: 10.1103/PhysRevFluids.2.100502
[18] Bechert DW, Bruse M, Hage W, et al. Fluid mechanics of biological surfaces and their technological application. Naturwissenschaften. 2000;87:157–171. doi: 10.1007/s001140050696
[19] Choi K-S. Near-wall structure of a turbulent boundary layer with riblets. J Fluid Mech. 1989;208:417–458. doi: 10.1017/S0022112089002892
[20] Walsh MJ. Riblets as a viscous drag reduction technique. AIAA J. 1983;21(4):485–486. doi: 10.2514/3.60126
[21] García-Mayoral R, Jiménez J. Hydrodynamic stability and breakdown of the viscous regime over riblets. J Fluid Mech. 2011;678:317–347. doi: 10.1017/jfm.2011.114
[22] Krieger V, Perić R, Jovanović J, et al. Toward design of the antiturbulence surface exhibiting maximum drag reduction effect. J Fluid Mech. 2018;850:262–303. doi: 10.1017/jfm.2018.423
[23] Modesti D, Endrikat S, Hutchins N, et al. Dispersive stresses in turbulent flow over riblets. J Fluid Mech. 2021;917:A55. doi: 10.1017/jfm.2021.310
[24] Abderrahaman-Elena N, García-Mayoral R. Analysis of anisotropically permeable surfaces for turbulent drag reduction. Phys Rev Fluids. 2017;2:Article ID 114609. doi: 10.1103/PhysRevFluids.2.114609
[25] Gómez-de-Segura G, García-Mayoral R. Turbulent drag reduction by anisotropic permeable substrates-analysis and direct numerical simulations. J Fluid Mech. 2019;875:124–172. doi: 10.1017/jfm.2019.482
[26] Rosti ME, Brandt L, Pinelli A. Turbulent channel flow over an anisotropic porous wall-drag increase and reduction. J Fluid Mech. 2018;842:381–394. doi: 10.1017/jfm.2018.152
[27] Choi K-S, Fujisawa N. Possibility of drag reduction using *d*-type roughness. Appl Sci Res. 1993;50:315–324. doi: 10.1007/BF00850564
[28] Silvestri A, Ghanadi F, Arjomandi M, et al. Attenuation of turbulence by the passive control of sweep events in a turbulent boundary layer using micro-cavities. Phys Fluids. 2017;29:Article ID 115102. doi: 10.1063/1.4995466

[29] Maa D-Y. Potential of microperforated panel absorber. J Acoust Soc Am. 1998;104(5):2861–2866. doi: 10.1121/1.423870
[30] Silvestri A, Ghanadi F, Arjomandi M, et al. Attenuation of sweep events in a turbulent boundary layer using micro-cavities. Exp Fluids. 2017;58(5):1–13. doi: 10.1007/s00348-017-2345-7
[31] Silvestri A, Ghanadi F, Arjomandi M, et al. Mechanism of sweep event attenuation using micro-cavities in a turbulent boundary layer. Phys Fluids. 2018;30:Article ID 055108. doi: 10.1063/1.5026130
[32] Scarano F, Jacob MC, Gojon R, et al. Modification of a turbulent boundary layer by circular cavities. Phys Fluids. 2022;34:Article ID 065134. doi: 10.1063/5.0091110
[33] Severino GF, Silvestri A, Cazzolato BS, et al. Sensitivity analysis of orifice length of micro-cavity array for the purpose of turbulence attenuation. Exp Fluids. 2022;63(24):1–10.
[34] Li M, de Silva CM, Chung D, et al. Modelling the downstream development of a turbulent boundary layer following a step change of roughness. J Fluid Mech. 2022;949:A7. doi: 10.1017/jfm.2022.731
[35] Bhat SS, Silvestri A, Cazzolato BS, et al. Mechanism of control of the near-wall turbulence using a micro-cavity array. Phys Fluids. 2021;33:Article ID 075114. doi: 10.1063/5.0051375
[36] Alster M. Improved calculation of resonant frequencies of Helmholtz resonators. J Sound Vib. 1972;24(1):63–85. doi: 10.1016/0022-460X(72)90123-X
[37] Chanaud RC. Effects of geometry on the resonance frequency of Helmholtz resonators. J Sound Vib. 1994;178(3):337–348. doi: 10.1006/jsvi.1994.1490
[38] Ingard U. On the theory and design of acoustic resonators. J Acoust Soc Am. 1953;25(6):1037–1061. doi: 10.1121/1.1907235
[39] Panton RL, Miller JM. Resonant frequencies of cylindrical Helmholtz resonators. J Acoust Soc Am. 1975;57(6):1533–1535. doi: 10.1121/1.380596
[40] Pierce AD. Acoustics – an introduction to its physical principles and applications. Woodbury (NY): ASA; 1989.
[41] Michelis T, de Koning C, Kotsonis M. On the interaction of Tollmien–Schlichting waves with a wall-embedded Helmholtz resonator. Phys Fluids. 2023;35:Article ID 034104. doi: 10.1063/5.0141685
[42] Michelis T, Putranto AB, Kotsonis M. Attenuation of Tollmien–Schlichting waves using resonating surface-embedded phononic crystals. Phys Fluids. 2023;35:Article ID 044101. doi: 10.1063/5.0146795
[43] Willey CL, Barnes CJ, Chen VW, et al. Multi-input multi-output phononic subsurfaces for passive boundary layer transition delay. J Fluids Struct. 2023;121:Article ID 103936. doi: 10.1016/j.jfluidstructs.2023.103936
[44] Dequand S, Hulshoff S, van Kuijk H, et al. Helmholtz-like resonator self-sustained oscillations, Part 2: detailed flow measurements and numerical simulations. AIAA J. 2013;41(3):416–423. doi: 10.2514/2.1992
[45] Ghanadi F, Arjomandi M, Cazzolato BS, et al. Analysis of the turbulent boundary layer in the vicinity of a self-excited cylindrical Helmholtz resonator. J Turbul. 2015;16(8):705–728. doi: 10.1080/14685248.2015.1024839
[46] Inagaki M, Murata O, Kondoh T, et al. Numerical prediction of fluid-resonant oscillation at low Mach number. AIAA J. 2002;40(9):1823–1829. doi: 10.2514/2.1859
[47] Ma R, Slaboch PE, Morris SC. Fluid mechanics of the flow-excited Helmholtz resonator. J Fluid Mech. 2009;623:1–26. doi: 10.1017/S0022112008003911
[48] Nelson PA, Halliwell NA, Doak PE. Fluid dynamics of a flow excited resonance, Part I: experiment. J Sound Vib. 1981;78(1):15–38. doi: 10.1016/S0022-460X(81)80156-3
[49] Stein L, Sesterhenn J. An acoustic model of a Helmholtz resonator under a grazing turbulent boundary layer. Acta Mech. 2019;230:2013–2029. doi: 10.1007/s00707-018-2354-5
[50] Bodart J, Scalo C, Shelekhov G, et al. Separation delay via hydro-acoustic control of a NACA-4412 airfoil in pre-stalled conditions. In: AIAA Paper 2017-1452; 2017.
[51] Yang SL, Spedding GR. Passive separation control by acoustic resonance. Exp Fluids. 2013;54(10):1–16. doi: 10.1007/s00348-013-1603-6
[52] Greenblatt D, Wygnanski IJ. The control of flow separation by periodic excitation. Prog Aerosp Sci. 2000;36:487–545. doi: 10.1016/S0376-0421(00)00008-7
[53] Seifert A, Bachar T, Koss D, et al. Oscillatory blowing: a tool to delay boundary-layer separation. AIAA J. 1993;31(11):2052–2060. doi: 10.2514/3.49121
[54] Seifert A, Greenblatt D, Wygnanski IJ. Active separation control: an overview of Reynolds and Mach numbers effects. Aerosp Sci Technol. 2004;8:569–582. doi: 10.1016/j.ast.2004.06.007
[55] Urzynicok F, Fernholz H-H. Flow-induced acoustic resonators for separation control. In: AIAA Paper 2002-2819; 2002.
[56] Panton RL, Miller JM. Excitation of a Helmholtz resonator by a turbulent boundary layer. J Acoust Soc Am. 1975;58(4):800–806. doi: 10.1121/1.380726
[57] Flynn KP, Panton RL. The interaction of Helmholtz resonators in a row when excited by a turbulent boundary layer. J Acoust Soc Am. 1990;87(4):1482–1488. doi: 10.1121/1.399445
[58] Flynn KP, Panton RL, Bogard DG. Effect of Helmholtz resonators on boundary-layer turbulence. AIAA J. 1990;28(11):1857–1858. doi: 10.2514/3.10490
[59] Panton RL, Flynn KP, Bogard DG. Control of turbulence through a row of Helmholtz resonators. In: AIAA Paper 1987-0436; 1987.

[60] Jafari A, McKeon BJ, Arjomandi M. Frequency-tuned surfaces for passive control of wall-bounded turbulent flow – a resolvent analysis study. J Fluid Mech. 2023;959:A26. doi: 10.1017/jfm.2023.149
[61] Baars WJ, Dacome G, Lee MK. Reynolds-number scaling of wall-pressure–velocity correlations in wall-bounded turbulence. J Fluid Mech. 2024;981:A15. doi: 10.1017/jfm.2024.46
[62] Willmarth WW. Pressure fluctuations beneath turbulent boundary layers. Annu Rev Fluid Mech. 1975;7:13–36. doi: 10.1146/fluid.1975.7.issue-1
[63] Gravante SP, Naguib AM, Wark CE, et al. Characterization of the pressure fluctuations under a fully developed turbulent boundary layer. AIAA J. 1998;36(10):1808–1816. doi: 10.2514/2.296
[64] Hultmark M, Smits AJ. Temperature corrections for constant temperature and constant current hot-wire anemometers. Meas Sci Technol. 2010;21:Article ID 105404. doi: 10.1088/0957-0233/21/10/105404
[65] Monkewitz P, Nagib HM. The hunt for the Kármán 'constant' revisited. J Fluid Mech. 2023;967:A15. doi: 10.1017/jfm.2023.448
[66] Hutchins N, Nickels TB, Marusic I, et al. Hot-wire spatial resolution issues in wall-bounded turbulence. J Fluid Mech. 2009;635:103–136. doi: 10.1017/S0022112009007721
[67] Smits AJ, Monty J, Hultmark M, et al. Spatial resolution correction for wall-bounded turbulence measurements. J Fluid Mech. 2011;676:41–53. doi: 10.1017/jfm.2011.19
[68] Segalini A, Orlu R, Schlatter P, et al. A method to estimate turbulence intensity and transverse Taylor microscale in turbulent flows from spatially averaged hot-wire data. Exp Fluids. 2011;51:693–700. doi: 10.1007/s00348-011-1088-0
[69] Liu C, Gayme DF. An input–output based analysis of convective velocity in turbulent channels. J Fluid Mech. 2020;888:A32. doi: 10.1017/jfm.2020.48
[70] Merino-Martínez R, Rubio Carpio A, Lima Pereira L, et al. Aeroacoustic design and characterization of the 3D-printed, open-jet, anechoic wind tunnel of Delft University of Technology. Appl Acoust. 2020;170:Article ID 107504. doi: 10.1016/j.apacoust.2020.107504
[71] Siebols R. Inner-scaled Helmholtz-resonators for turbulent boundary layer flow control [M.Sc. thesis]. Delft, The Netherlands: Delft University of Technology, 2022 Jun.Available from: http://resolver.tudelft.nl/uuid:df53a98f-8d70-4d58-b578-1ce804d8c1ac.
[72] Klewicki JC, Priyadarshana PJA, Metzger MM. Statistical structure of the fluctuating wall pressure and its in-plane gradients at high Reynolds number. J Fluid Mech. 2008;609:195–220. doi: 10.1017/S0022112008002541